OPEN ACCESS



A Gradual Decline of Star Formation since Cluster Infall: New Kinematic Insights into Environmental Quenching at 0.3 < z < 1.1

Keunho J.Kim¹, Matthew B. Bayliss¹, Allison G. Noble^{2,3}, Gourav Khulla⁴, Ethan Cronk⁶, Joshua Roberson Behzad Ansarineja, Lindsey E. Bleem, Benjamin Floyd, Sebastian Grandis, Guillaume Mahler, Michael A. McDonald, Christian L. Reichard, Alexandro Saro, Keren Sharoh, Keren Sharoh, Taweewat Somboonpanyakup, and Veronica Strazzull 5,1900 ¹ Department of PhysicsUniversity of Cincinnati, Cincinnati, OH 45221, USA; kim2k8@ucmail.uc.edu School of Earth and Space ExploratioArizona State UniversityTempe,AZ 85287, USA Beus Center for Cosmic Foundation&rizona State UniversityTempe,AZ 85287, USA ⁴ Department of Physics and Astronomy and PITT PACOniversity of Pittsburgh,Pittsburgh,PA 15260,USA ⁵ Kavli Institute for Cosmological Physics Iniversity of Chicago, 5640 South Ellis Avenue Chicago, IL 60637, USA ⁶ Kavli Institute for Astrophysics & Space Researd Massachusetts Institute of Technolog √7, Massachusetts Avenu€ambridge MA 02139, USA School of Physics University of Melbourne Parkville, VIC 3010, Australia Argonne National LaboratoryHigh-Energy Physics Division9700 South Cass Avenuergonne, IL 60439, USA Department of Physics and Astronomyniversity of Missouri–Kansas CityKansas CityMO 64110, USA Faculty of PhysicsLudwig-Maximilians-UniversitätScheinerstr1, D-81679 Munich, Germany 11 Institute for Computational Cosmolog@urham University.South RoadDurham DH1 3LE,UK
12 Centre for Extragalactic AstronomPurham University South RoadDurham DH1 3LE,UK Centre for Extragalactic Astronom Durham University South Road Durham DH1 3LE, UK Astronomy Unit, Department of Physics Iniversity of Trieste, via Tiepolo 11, I-34131 Trieste Italy IFPU—Institute for Fundamental Physics of the University Beirut 2, I-34014 Trieste Italy INAF—Osservatorio Astronomico di Trieste la G.B. Tiepolo 11, I-34143 Trieste la INFN—National Institute for Nuclear Physics (ia Valerio 2, I-34127 Trieste la Ivalerio 2, Ivaler ¹⁷Department of AstronomyUniversity of Michigan,1085 South University AvenueAnn Arbor, MI 48109, USA ¹⁸Kavli Institute for Particle Astrophysics & Cosmology (KIPAC),52 Lomita Mall, Stanford,CA 94305,USA 19 INAF—Osservatorio Astronomico di Brerà/ia Brera 28,20121 Milano, Via Bianchi 46, I-23807 Merate, Italy Received 2022 June 9; revised 2023 July 14; accepted 2023 July 27; published 2023 September 14

Abstract

The environments where galaxies reside crucially shape thetar formation histories. We investigate a large sample of 1626 cluster galaxies located within 105 galaxy clusters spanning a large range in redshift (0.26 < z < 1.13). The galaxy clusters are massive $(\overline{\mathbb{M}} \ 2 \times 10^4 \, \mathrm{M}_{\mathrm{e}})$ and uniformly selected from the SPT and ACT Sunyaev-Zel'dovich surveysWith spectra in hand for thousands of cluster members use the galaxies' position in projected phase space as a proxy for their infall times, which provides a more robust measurement of environmentthan quantities such as projected clustercentric radiuse find clear evidence for a gradual age increase of the galaxy's mean stellar populations (~0.71 ± 0.4 Gyr based on a 4000 Å bteal000) with the time spent in the cluster environment. This environmental quenching effect is found regardlessof galaxy luminosity (faint or bright) and redshift (low or high-z), although the exact stellar age of galaxies depends on both parameters at fixed environmental effects. Such a systematic increase 00000 with infall proxy would suggest that galaxies that were accreted into hosts earlier were guenched earlier due to longer exposure to environmental effects such as ram pressure stripping and starvation. Compared to the typical dynamical timescales of 1-3 Gyr of cluster galaxies, the relatively small age increase (~0.71 ± 0.4 Gyr) found in our sample galaxies seems to suggest that a slow environmental process such as starvation is the dominant quenching pathway. Our results provide new insights into environmental quenching effects spanning a large range in cosmic time (~5.2 Gyr, z = 0.26–1.13) and demonstrate the power of using a kinematically derived infall time proxy.

Unified Astronomy Thesaurus concepts: Galaxy clusters (584); High-redshift galaxy clusters (2007); Galaxy quenching (2040); Galaxy evolution (594); Galaxy environments (2029); Galaxies (573)

1. Introduction: A Kinematic Method for Investigating Environmental Quenching at High-z

The environment where galaxies reside is closely linked to the galaxies' characteristic bolding key information for their evolutionary histories. In particular, cluster environments have ments of clusters have indeed affected the residing galaxies shown remarkably tight relationships with the fundamental properties of galaxies, such as morphology (Dressler 1980; Ohram pressure stripping (Gunn & Gott 1972; Abadi et 1989); et al. 2018), star formation rate (SFRPark & Hwang 2009;

Original content from this work may be used under the terms of the Creative Commons Attribution 4.0 licence. Any further distribution of this work must maintain attribution to the author(s) and the title of the work, journal citation and DOI.

Noble et al. 2013; Muzzin et al. 2014), and gas components (e.g., Kenney et al. 2004: Chung et al 2009).

Such close relationships between cluster environments and galaxy properties suggesthat the extremely dense environthrough various effects, such as hot intracluster medium (ICM) Ebeling et al. 2014; Boselli et al. 2022), strangulation (starvation; Larson et al. 1980), harassment(Moore et al. 1996), and tidal interactions (Byrd & Valtonen 1990).

In particular, these environmental effects are known to efficiently suppress (aka quench) the star formation activity of cluster galaxies. Indeed, the higher fraction of guiescent

galaxies in clusters compared to field environments (Pintos-Castro et al. 2019; Strazzullo et al. 2019; Paulino-Afonso et al. rates (sSFRs) of galaxies as a function of the infall time proxy 2020) and systematically truncated das disks found in Local cluster galaxies (e.g., the Virgo cluster; Yoon et al. 2017) suggest the cluster environmental "quenching" effects at play. observationalenvironmentalmeasurefor infall time. Later

Universe (z < 0.2), where a wealth of clusters have been observed and analyzed in detail (e.g., Oh et al. 2018; Pasquali similar method using projected phase space. et al. 2019; Smith et al. 2019; Boselli et al. 2022; Cortese et al. 2021; Morokuma-Matsui et al. 2021; Upadhyay et al. 2021, for environmentalquenching effects than the projected distance a review). The decreasing number of clusters and the reduced alone at high redshifts by crucially utilizing the advanced brightness with increasing redshift make it challenging to studykinematic approach over a huge range in cosmic time high-redshift cluster populations. While several studies have Universe (e.g., Strazzullo et al. 2013; Pintos-Castro et al. 2019effect (Sunyaev & Zeldovich 1972) from the South Pole Kelkar et al. 2019; Khullar et al. 2021; Webb et al. 2020; Balogh et al. 2021; Noordeh et al. 2021; Reeves et al. 2021), only a relatively small number of clusters at high redshift (z □ 0.4) have been studied in detail for environmental quenching effects with spectroscopically confirmed member galaxies (e.g.Muzzin et al. 2012; Tiley et al. 2020; Vaughan et al. 2020; Balogh et al. 2021; Matharu et al. 2021). Furthermore, most studies at high redshift use the galaxies' projected distance from the cluster center as a primary the projected clustercentric distance is a usefulvironmental parameter, it inevitably suffers from contamination from interlopers that happen to lie within the cluster's projected radius but in turn are unrelated to the host cluster.

Notably, by adopting an advanced environmentalmetric based on the cluster galaxies information, our study attempts to minimize the contamination from projected interlopers. Thus, our study enables us to investigate in detail how the star formation of galaxies changes ovetime since infall into the host cluster. Specifically, we estimate the galaxies' infall stages (ranging from recently accreted populations to early ancient infallers) by putting together their clustercentricdistance and peculiar velocity relative to the cluster center.

This "phase space" (i.e.,the diagram of the clustercentric distance versus the peculiar velocity normalized by the velocity environmental effects on galaxy properties in a uniform way infall histories of cluster galaxiessince it considers not only the distance from the clustercenter but also the "kinematic" velocity of infalling galaxies. Numerous clustersimulations, where the galaxies' time steps can be traced, have indeed demonstrated the clearseparations galaxies by different infall stages in phase space (Mahajan et 20.11; Oman et al. 2013; Muzzin et al. 2014; Haines et al. 2015; Jaffé et al. 2015; Oman & Hudson 2016; Rhee et a2017, 2020).

Motivated by the simulation results everal studies utilized the projected phase space (i.e., the projected clustercentric radius and the line-of-sighteculiar velocity used instead) for actual cluster galaxies to estimate the galaxies' orbitalages over a wide range of redshiftsoth local (e.g., Vollmer et al. 2001; Mahajan etal. 2011; Boselli et al. 2014b; Hernández-Fernández et al. 2014; Haines et al. 2015; Gavazzi et al. 2018; subsequently followed up with optical/near-IR imaging to Jaffé et al. 2018; Shen et al. 2020; Loni et al. 2021; Reeves et al. 2023) and high-redshift clusters (e. Noble et al. 2013; Muzzin et al. 2014; Liu et al. 2021). In particular, Noble et al. (2013) estimated the infall time of galaxies in a $z \sim 0.9$ cluster, discovered in the surveys aredshifts z = 0.1-1.5The cluster

They found a systematic decrease of the specific star formation derived from the galaxies' location in the projected phase space, suggesting the projected phase space as a robust However, no clear consensus about the environmental effectstudies in the local Universe (z < 0.2; e.g., Pasquali et al. 2019; has been established yet at high redshifts, contrary to the localSmith et al. 2019; Sampaio et al. 2021) support this by showing a similar trend of reduced sSFR of cluster galaxies based on a

The goal of our study is to provide a clearer view of the (\sim 5.2 Gyr, z = 0.26–1.13). For that, we employ a large number indeed investigated the environmental effects outside the local of clusters uniformly selected by the Sunyaev-Zel'dovich (SZ) Telescope (SPT; Bleem et a 2015) and Atacama Cosmology Telescope (ACT; Marriage et al. 2011) cluster surveys. We obtain the photometric and spectroscopic information of cluster galaxies from the optical follow-up observations of the SZ clusters (Ruelet al. 2014; Bleem et al. 2015; Bayliss et al. 2016, and references therein).

Section 2 describes the observation data sets. The sample selection procedure and data analysis are described in Section 3. We present and discuss our results in Section 4. environmental measure for quenching effects in clusters. While We summarize our conclusions with final remarks in Section 5. the projected clustercentric distance is a use-finite variable. We adopt the Ω DM cosmology of ($\frac{1}{10}$, Ω_m , Ω_Λ) = (70 km s⁻¹) Mpc^{-1} , 0.3, 0.7) throughout the paper.

2. The Observational Data Sets

We use observationadata sets drawn from the 2500 deg SPT-SZ (Vanderlinde et al. 2010; Reichardtet al. 2013; Ruel et al. 2014; Bleem etal. 2015; Bayliss et al. 2016, 2017) and ACT-SZ (Marriage etal. 2011; Hasselfield etal. 2013; Sifón et al. 2013) cluster surveys and the associated optical/near-IR follow-up observations. Due to the redshift independence of the SZ effect, the clusters identified by these surveys are nearly mass-limited with a mass threshold of □3 × 10 ⁴ Me at all redshifts (see, e.g., Figure 6 of Bleem et al. 2015). This uniform cluster selection function through the SZ effect, combined with the uniform selection of the galaxy samples, allows us to study dispersion of the cluster) is a powerful tool to study the detailed over a wide range of redshifts (0.26 < z < 1.13). In this section, we describe the details of the cluster surveys (Section 2.1), the galaxy photometric i-band luminosity (Section 2.2) and the spectral 4000 Å break measurements (Section 2.3).

2.1. Clusters Uniformly Selected by the SZ Effect from SPT and ACT at 0.26 < z < 1.13

Our sample of clusters is a subsample of the clusters identified in the 2500 deg² SPT-SZ (Reichardtet al. 2013; Bleem et al. 2015) and ACT-SZ surveys (Marriage et al. 2011; Hasselfield etal. 2013). We refer the reader to the aforementioned publications for full descriptions of these surveys In short, these cluster candidates were first detected through their SZ signal (i.e., the SZ signal-to-noise threshold $\xi \square 4.5$) and confirm the clusters associated with the SZ sign/albout 500 clusters (415 and 68 from the SPT and ACT, respectively, with some overlapping clustersbetween the surveys)have been

masses—Mo the mass measured within the radius \$00 at which the mean density of the cluster is 500 times the critical density at the cluster redshift—are □3 × 10⁴ M_e, nearly independent of redshift due to the selection function based on the SZ effect.

From the surveys, we adopt information about the cluster center, redshift (z_{cl}), and mass (M₅₀₀) of our 105 sample clusters at 0.26 < z_I < 1.13 (see Section 3.1 for details about sample selection). Specificall99 clusters from SPT and nine from ACT satisfy these criteria, with three clusters appearing in We use the i-band luminosity, Uscaled by L, L,/L*, as our both catalogs. The result is a total sample of 105 SZ-selected galaxy clustersFor the three clusters in both catalogue use the SZ information from SPT alone (there are no published scaling relations for a combination of SPT and ACT SZ data, but see Hilton et al. 2018 for a discussion of ACT and SPT mass consistency). In particular, the cluster mass (M₅₀₀) is SPT clusters measured from Reichardtal. 2013 and Bleem et al. 2015 and six ACT clusters measured from Hasselfield et al. 2013). For the SPT clusters, the following scaling relationon analytic fits to the Red-sequence ClusterSurvey 2 data is used:

$$z = A_{SZ} \left(\frac{M_{500}}{3 \cdot 10^{14} M_{\Box} h^{-1}} \right)^{B_{SZ}} \left(\frac{H (Z)}{H (0.6)} \right)^{C_{SZ}}, \tag{1}$$

where Az is the normalization factor. B is the slope, and G is the redshift evolution term associated with the Hubble parameterH(z). Here ζ is the unbiased SZ significance δ^0 associated with the SZ signal-to-noise threshold ξ as follows:

$$z = \sqrt{\dot{a}x \, \hat{n} - 3} \ . \tag{2}$$

The values of A_{SZ} , B_{SZ} , and C_{SZ} are 4.14, 1.44, and 0.59, respectively as determined in Reichardtt al. (2013). For the six ACT clusters, we adopt the SZ signal based-cluster mass that is calibrated with the cluster physics model of Bode et al. (2012) in Hasselfield et al. (2013; see Section 3.4 and Table 10the luminosity-weighted mean stellarage of galaxies. The of Hasselfield et al2013 for more details).

Further details on the cluster surveys, such as cluster identification and mass estimates, can be found in Bleem et al. (2015) and Hasselfield et al. (2013) for the SPT and ACTwavelength (Bruzual 1983; Hamilton 1985; Balogh et al. clusters, respectively.

2.2. Galaxy i-band Luminosity Relative to the Characteristic Luminosity (L/L*) for Photometric Brightness

We obtain the i-band luminosity (Lof our sample galaxies from the optical follow-up observations of the SPT cluster surveys (Bleem et al2015, 2020, and references therein) that are conducted to confirm the clusters associated with the SZ signal. Severaldifferent telescopes are used for the follow-up observations (see Table 2 of Bleem et al. 2015; for more recent observations with the PISCO instrumen Stalder et al. 2014, see Section 4 of Bleem et al. 2020), including the Blanco/ MOSAIC-II; Magellan/Baade IMACS f-2; Magellan/Clay LDSS3, Megacam, and PISCO; Swope/SITe3; MPG/ESO WFI; and New Technology Telescope/EFOSC2.

While the aperture size of the telescopes is notthe same (1-6.5 m), we note that the follow-up campaign is optimally designed to observe clusters with uniformly sufficient depth at both low (z \square 0.3) and high (z \square 0.75) redshifts. Typically, the

sample galaxies' photometric brightne se adopt the i-band L values computed in the SPT-SZ surveys (High et 20.10; Bleem et al. 2015). Specifically, Lis derived using the stellar population synthesis modelf Bruzual & Charlot (2003), and the stellar population modeling assumes a k-corrected, passively evolvinginstantaneous-burst stellar population with derived from the SZ signal-cluster mass scaling relation (for 99a formation redshift of z = 3. The Salpeter initial mass function (Salpeter 1955) and the Padova 1994 stellar evolutionary tracks (Fagotto et al.1994) are usedMetallicities are selected based (Gilbank et al. 2011). Interpolation using cubic splines is applied to generate L values at redshifts where the stellar synthesis modedid not directly compute L. The models are further calibrated to the actual SPT spectroscopic subsample. A comparison shows that the computed our sample cluster galaxies is in good agreement with that of the maxBCG cluster sample of Rykoff et al. (2012). Specifically, the L* values between the two studies are consistently better than □5% over the overlapping redshiftrange at z = 0.05-0.35. As we will describe in Section 3.1, we use galaxies brighterthan 0.35 L_i/L * as our sample galaxies across alredshifts of interest (0.26 < z < 1.13).

2.3. The Age-sensitive 4000 Å Break (40000) for the Mean Stellar Age of Galaxies

We use the 4000 Å break strength (£000) as a proxy for D_n4000 is a spectral feature that arises from the accumulation of the metal absorption lines of stars making a "break" between the blue- and red-side continua around 4000 Å in rest-frame 1999). Because the metal absorption line strength is sensitive to stellar type (i.e., age given surface gravity and temperature), D_n4000 is sensitive to the luminosity-weighted mean stellar age of galaxies. Thus, \$\overline{\pi}4000\$ has been widely adopted as a useful stellar age indicator of galaxies (Kauffmann et al. 2003, 2004; Hernán-Caballero et al. 2013; Geller et al. 2014; Haines et al. 2017; Kim et al. 2018, and reference therein).

The D_14000 is defined as the average flux density ($\langle F \rangle$) ratio between the blue-side (答) and the red-side ((的) continua

$$\acute{a}F\tilde{n} = \frac{\grave{Q}_{1}^{I_{2}}F_{n}dI}{\grave{Q}_{1}^{I_{2}}dI};$$
(3)

thus, D_n4000 is expressed as

$$D_{n}4000 = \frac{\acute{a}F^{R}\tilde{n}}{\acute{a}F^{B}\tilde{n}} = \frac{(I_{2}^{B} - I_{1}^{B}) \grave{Q}_{R}^{I_{2}^{B}} F_{n} d I}{(I_{2}^{R} - I_{1}^{R}) \grave{Q}_{B}^{I_{2}^{B}} F_{n} d I},$$
(4)

observations are required to detect 0.4L* galaxies with 5σ depth, where Lis the characteristic luminosity of galaxies at a given redshift. The majority of the photometry uses the Sloan Digital Sky Survey (SDSS) i-band filter. For clusters observed with the older Johnson-Cousins photometric BVRI system, the filter transformation of the I band into the SDSS i band is applied in Bayliss et al. (2016; see their Section 5.2). As a result, all of our sample galaxies'is measured with respect to the SDSS i-band filter.

²⁰ See Appendix B in Vanderlinde et a(2010) for details.

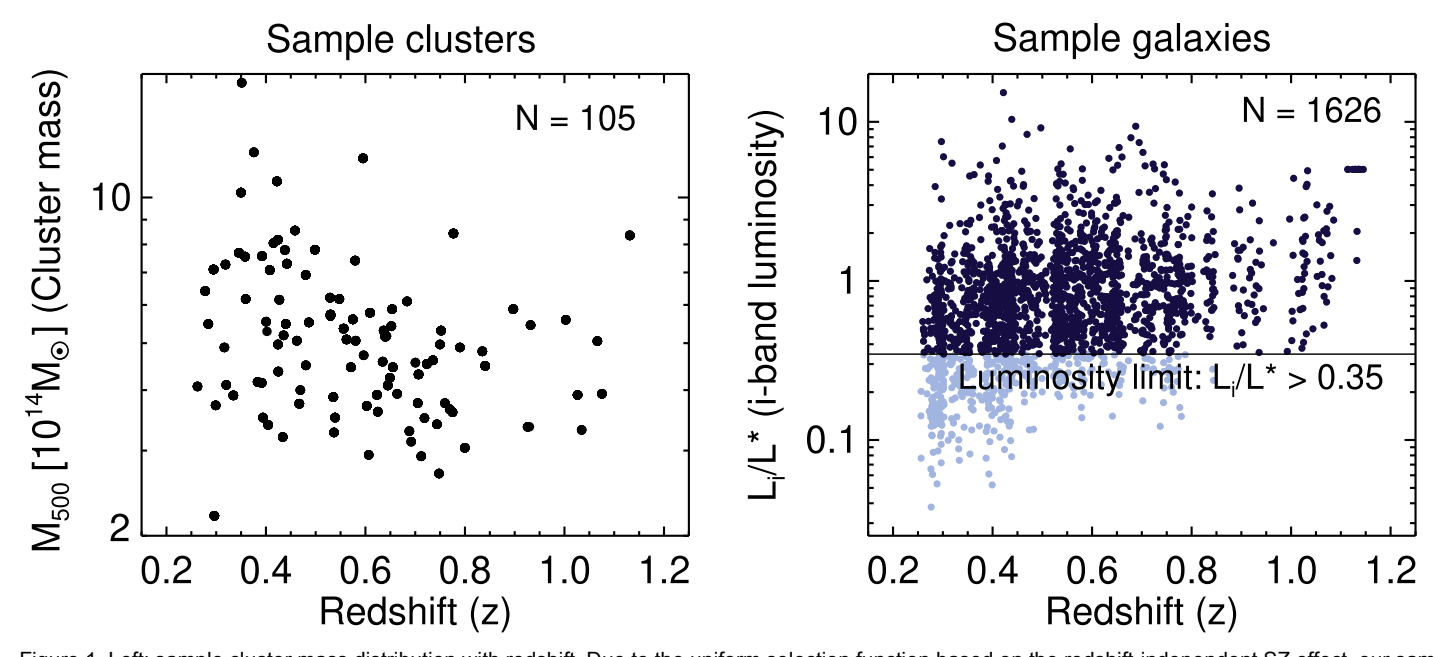


Figure 1. Left: sample cluster mass distribution with redshift. Due to the uniform selection function based on the redshift-independent SZ effect, our sample clusters are nearly mass-limited at all redshifts, forming a relatively narrow mass range with a median (standard deviation) mass of 4.9% (120.124Mg, (Section 2.1). Right: i-band luminosity (L/L*, relative to the characteristic luminosity) distribution of sample cluster galaxies with redsified dark blue points are the sample galaxies used after applying the luminosity cut, the L > 0.35, while the light blue points are the ones excluded. The numbers of sample clusters and cluster galaxies considered in this study are marked in the top right corner in the left and right panels, respectively. See also Table 1 and Section 3.1 for details on the sample sele

D_n4000 increases with galaxy age such that galaxies with young stellar populations (□1 Gyr) show4D00 □ 1.5, while galaxies with old stars (□1 Gyr) show 40000 □ 1.5 based on simple stellar population modelings (see, e.g., Figure 2 of Kauffmann et al.2003).

We obtain the \$\text{\$\pi\}4000\$ of our sample galaxies measured from foreground galaxies. the optical follow-up spectroscopic observations SPT-SZ therein) and ACT-SZ (Sifón et al. 2013) clusters. Most clusters practical given the observational resource costso it is not a (Ruel et al. 2014; Bayliss et al. 2016, 2017, and references are observed with the GeminiMulti-Object Spectrograph on Gemini South, IMACS on Magellan/Baade, or FORS2 on the Very Large Telescope. The observations are primarily designed by D_n4000 of the complete sample of SPT cluster member to measure spectroscopic redshifts galaxies for accurate cluster membershipsthrough the cluster velocity dispersion (σ_{cl}) .

The specific observing strategy (e.g., target selection, multislit mask design and the choice of grating and filter) is set up to uniformly observe a large number (\square 100) of clusters strategy was applied uniformly, any systematic D_n4000 The spectroscopic integration times for individual masks were computed to ensure that the signal-to-noise ratio is $\square 3$ spectra(e.g., galaxy luminosity, redshift, and environment) should be pixe¹ in the continuum around D₀4000 based on a model passive galaxy spectrum with a brightness equal to: L4 at luminosity range (see the right panel of Figure 1).

The target selection is based on the color-magnitude diagram of galaxies observed in the field of view of a given cluster. The highest priority is given to cluster galaxies identified by the red sequencegardless of luminositydown to ;0.4 L _i/L*. We first identified the red sequence as an overdensity in color and then fit a tilted red sequence to the daterming) fractions of ~70% (30%) and ~66% (34%) for lowin color-magnitude.Likely red-sequence galaxies were those galaxies within ±0.15 mag (in color) of the best-fit red sequence. The choice of ±0.15 mag corresponds to ±2.5–3 σ_{RS} , where σ_{RS} is the intrinsic width of the observed

red sequence, which has been measured to be ;0.05 mag for massive galaxy clusters (Hennig et al. 2017). The next highest priority is given to candidate "blue cloud" galaxies hich are identified as those galaxies that are bluer than the red sequence (i.e., star-forming). We also only include galaxies that are fainter than the brightest red-sequence member filter out

Obtaining spectroscopic follow-up of a complete sample of cluster galaxies in hundreds of distant galaxy clusters is not realistic possibility to measure D_n4000 for every cluster member galaxy in our cluster samplehis limitation prevents us from interpreting our results as an absolute measurement of galaxies. That said, we note that the slit placement strategy that produced our spectroscopic membesample was uniformly applied to all spectroscopic observationwith no systematic evolution in the radial density of the spectroscopic slits or the rest-frame magnitude limits. Because the slit placement difference within our sample that scales with other parameters robust.

Understanding our spectroscopic galaxy sample selection is the cluster redshift. Note that we quite consistently sample this essential to interpreting our results, so we also perform a direct comparison of our spectroscopiccluster member sample againsta published photometric analysis that ses complete cluster galaxy populations. Specifically, we measure the fractions of passive (red sequence) and star-forming (blue cloud) cluster member galaxies in our final spectroscopic catalog in our two redshift bins. We measure passive (starredshift ($\langle z \rangle$ of 0.41) and high-redshift ($\langle z \rangle$ of 0.66) clusters, respectively. These fractions are consistent the observed red/passive galaxy fraction measured for all SPT clusters using photometric data (Hennig et al. 2017; see their Figure 15). The

Table 1 Summary of Sample Selection (Section 3.1)

Criterion Cross-matching the cluster catalog and optical photometric and spectroscopic follow-up catalogs	Explanation/(Number of Galaxies) To obtain cluster mass (\(\\ \\ \ \ \ \ \ \ \ \ \ \ \ \ \ \	
$0.7 < D_n 4000 < 2.3$ and $\sigma(D_n 4000)/D_n 4000 < 0.3$	To remove the poor or missing measurements o#1000 due to wavelength coverage of observed spectra/(2709)	
0.26 < z < 1.13	Redshift range divided into low-z $(0.26 < z < 0.53)$ and high-z $(0.53 < z < 1.13)$ bins with 46 and 59 clusters; spectively	
$L_i/L^* > 0.35^b$	Galaxy luminosity cut to ensure a uniform lower limit of galaxy luminosity at all redshifts/(2125)	
Cluster member galaxies $ \Delta v /\sigma_{cl} < 3.5$ and r $_{pro}/r_{500} < 3$	Membership based on the normalized line-of-sight peculiar velocity (Δωβν and projected clustercentric radius, (ε/ς ₅₀₀)/ (1626: 802 and 824 in low- and high-z binsespectively)	
Total number in sample	105 clusters and 1626 member galaxies	

Notes.

consistency between the passive and star-forming fractions in $\sigma(D_n 4000)/D_n 4000$ (relative error) < 0.3, our spectroscopiccatalog and published imaging analyses indicates that the sparsespectroscopicsampling does, on

Typically, N

40 galaxiesper cluster are observed. The observed spectracover a galaxy rest-frame wavelength of ;3500–5150 Å across redshifts z ; 0.25–1.1. The observations have a similar spectral resolution, dR□; 5–10 Å, corresponding sample galaxies to ensure a uniform lower limit to R ($=\lambda/d\lambda$); 500–1200. The observed spectroscopy is used to measure D4000 by Bayliss et al. (2016) using the same definition given in Equations (3) and (4).

We refer the reader to the spectroscopic follow-ups of SPT-SZ clusters (Ruelet al. 2014; Bayliss et al. 2016, 2017) for more details about the observing strategy and the D_n4000 measurements.

3. Sample Selection and Data Analysis

Galaxies at 0.26 < z < 1.13

We select our sample clusters by cross-matching the SZ cluster catalog and the opticaphotometric and spectroscopic follow-up catalogs described in Section 2. From the crossmatch, we obtain the clustermass (M₅₀₀), galaxy luminosity (L_i/L⁻), D_n4000, and cluster velocity dispersion_i)(σThere are 105 clusters and 4089 galaxies in ourinitial sample with a redshift ranging from 0.26 to 1.13.0f the 105 clusters99 of The cluster mass range is 3 × 100M_e □ M₅₀₀ □ 3 × 10⁵ M_e with a median mass of 4.97 \times 10 $^{\circ}$ M_e and an associated 1 σ population spread of ±2.24 × 10 M_e. The mass distribution of our sample clusters is shown in the left panel of Figure 1.

Sampling galaxies with reliable D ,4000 measurement is crucial in our analysis. We apply additional sample selection criteria based on physically reasonable \$\overline{\mathbb{P}}4000 values from spectra suffer from data reduction artifacts (e.g., bright sky line residuals), as well as high noise. Specifically, we select galaxies whose D_n4000 satisfies 0.7 < $D_{n}4000$ <

leaving 2709 galaxies. The D_n4000 range selected reasonably coverthe observed D4000 strengths across attypes of galaxies from average, recover a representative population of cluster galaxie young (~10 Myr) to old (~15 Gyr) stellar ages based on simple stellar population modeling (e.g., Kauffmann et al. 2003; Hernán-Caballero et al. 2013).

We also apply a luminosity cut of $L_i/L^* > 0.35$ to the galaxy luminosity at all redshifts. Specifically, we derive the luminosity cut by considering the 10th percentile (i.eabove which 90% of the population lies) of the L distribution of our high-redshift (0.53 < z < 1.13) subsamples. This corresponds to 0.35 of L_i/L^* , which is very similar to the typical depth (5σ for 0.4L) of the photometric follow-ups of SPT-SZ clusters (Bleem etal. 2015). We thus remove galaxies with L_i/L * < 0.35, leaving 2125 galaxiesThe L_i/L * distribution of our sample galaxies with the luminosity $cut(L_i/L^* > 0.35)$ 3.1. Sample Selection: A Uniform Set of 105 Clusters and 1626applied is shown in the right panel of Figure 1. Title Lrange sample galaxies roughly corresponds to 10.3 $\log(M_{\rm star}/M_{\odot})$ 11.6, given the typical characteristic stellar mass of 0.8 \square log($M_{\text{star}}/M_{\square}$) (e.g., Adams et al. 2021)

Lastly, of 2125 galaxies,499 galaxies are further removed based on their projected cluster centric radius (ro/r 500) and the normalized line-of-sight peculiar velocity ($\Delta v/\sigma_{cl}$; them are SPT clusters, and the remaining six are ACT clustersEquation (5)). This criterion is applied to select cluster member galaxies with reasonable orbital stages (i.e., |Δy#6.5 and r_{pro/}r₅₀₀<3), as we will describe in detail in Section 3.2.

at similar redshifts and an I-band mass-to-light ratio of 0.8-2.5

(e.g., McGaugh & Schombert 2014).

In total, our final sample throughout the paper is 105 clusters and 1626 galaxies at 0.26 < z < 1.13. On average, 15 galaxies cluster are sampled. The typical uncertainty in cluster mass in our cluster sample is 0.9 × 110M_e, and the typical uncertainty in the i-band photometry of cluster membergalaxies is 0.06

a The catalogs for SPT-SZ (Reichardt et al013; Bleem et al. 2015) and ACT-SZ (Hasselfield et al013) clusters and the optical photometric (High et al010; Bleem et al.2015) and spectroscopic (Sifón et al013; Ruel et al.2014; Bayliss et al.2016, 2017) follow-ups (Section 2).

b Luminosity cut of L/L > 0.35 estimated from the 90th percentile of the high-z subsamples (Section 3.1 and the right panel of Figure 1).

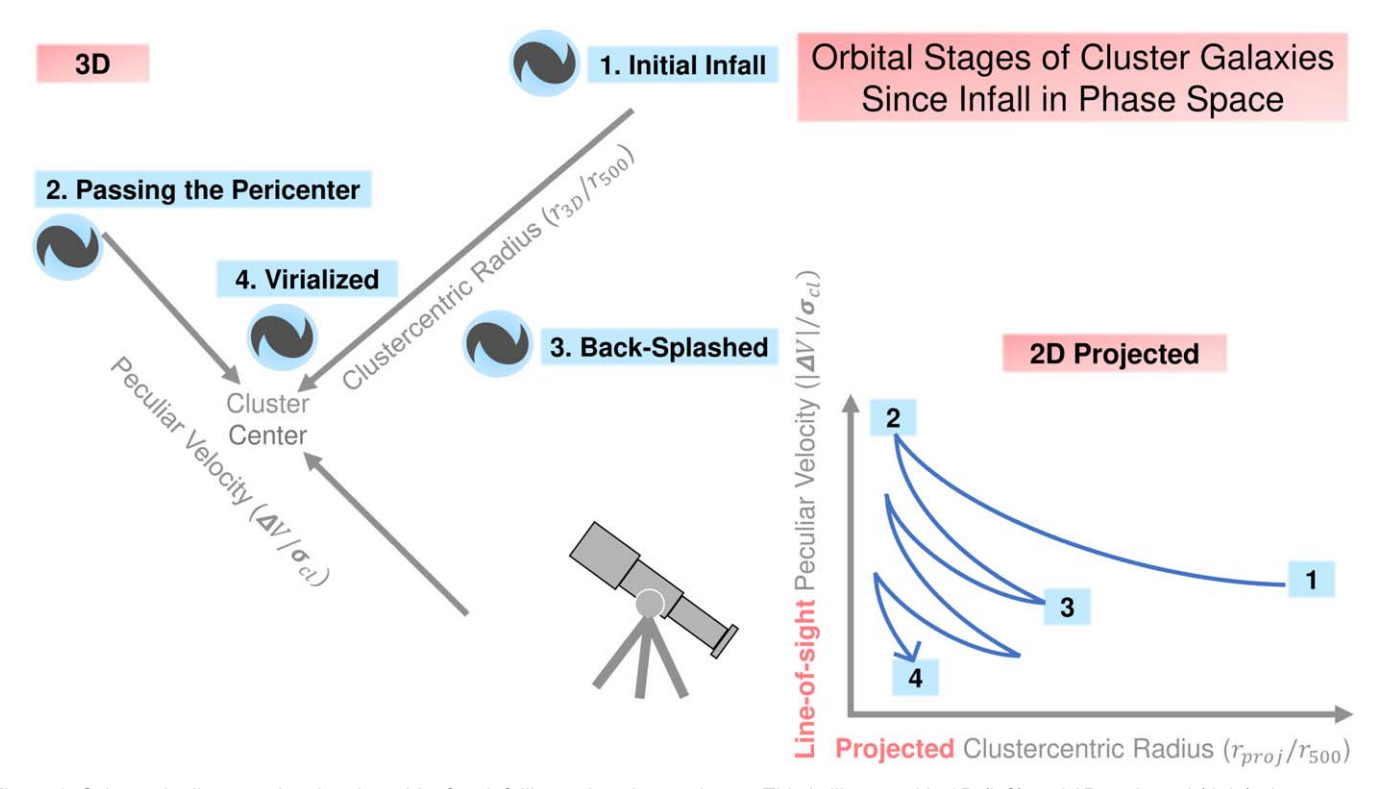


Figure 2. Schematic diagram showing the orbit of an infalling galaxy into a cluster. This is illustrated in 3D (left) and 2D projected (right) phase space (i.e., peculiar velocity vs. clustercentric radius). Moving from stages 1 to 4, (1) an infalling galaxy plunges into the gravitational potential of the cluster, (2) passes the pericenter, backsplashes, and Deventually becomes (4) virialidedsimplified orbit of an infalling galaxy is qualitatively consistent with that of an infalling galaxy traced in cluster simulations (e.g., see Figure 4 of Jaffé et al. 2015). This figure illustrates how a galaxy orbit is statistically traced in a phase space diagram during infall (see also Figure 3 for the projected phase space of our sample galaxies).

3.2. Kinematically Estimating the Infall Time of Galaxies from Projected Phase Space

location in the phase space, similar to other studies (Noble et al. (2019) shows that galaxies We estimate the infall time of galaxies based on their 2013, 2016; Pasquali et al. 2019). The phase space is a diagrammed show systematically different mean infall times, as where the infall stage of cluster galaxies can be kinematically estimated (Figure 2). It uses the clustercentric distance and peculiar velocity normalized by cluster velocity dispersion on its axes. For the projected phase space, the projected clustercentric distance_p(6/r 500) and the line-of-sight peculiar velocity normalized by the cluster velocity dispersion (Δy)σ are employed.

Indeed, cluster simulations where the infall stages of galaxies can be traced have demonstrated that alaxies distinctively occupy differentlocations of phase space depending on their infall time (Mamon et al. 2004; Gill et al. 2005; Mahajan et al. 2011; Haines et al. 2012; Oman et al. 2013; Rhee et al. 2017) Typically, galaxies that were accreted early show a wide range early. The intermediate infallzone contains a mix of galaxy of peculiar velocities $(\Delta v/\sigma_1)$ at small clustercentric distances (r/r 500) but only populate small peculiar velocities over larger clustercentric distancen contrast, galaxies that were accreted recently are distributed over ranges of clustercentric distance and peculiar velocity but preferentially distributed following trumpet-like profiles that can be described by lines of constant $(r/r_{500}) \times (|\Delta v|/\sigma_{cl})$ (see, e.g., Figure 3 of Haines et al. 2012).

Motivated by these phase space trends with infatime in simulations, Noble et al. (2013) observationally utilized the caustic lines—the trumpet-shaped lines $(r_{proi}/r_{500}) \times (|\Delta v|/\sigma_{cl}) = constant (see also Figure 3)—of$ (Noble et al. 2016; Pasqualiet al. 2019) demonstrated the utility of the caustic lines as a useful infall time proxy for cluster galaxies. In particular, a comparison with cluster eparated by the caustic linesin the projected phase space described below.

We adopt the same definition of infall time zones based on the location of phase space as in Noble et al. (2013), which is as

- 1. early infall, (r $_{proj}$ /r $_{500}$) × ($|\Delta v|/\sigma$ $_{cl}$) < 0.1; 2. intermediate infall,0.1 < (r $_{proj}$ /r $_{500}$) × ($|\Delta v|/\sigma$ $_{cl}$) < 0.4;
- 3. recent infall, $(r_{proi}/r_{500}) \times (|\Delta v|/\sigma_{cl}) > 0.4$.

As the names of each infall zone indicate, the early infall zone primarily consists of virialized galaxies that were accreted populations with intermediate infallers, as well as a backsplash population that has passed the firstcluster pericenterand is currently outbound. The recent infall zone is mainly populated by galaxies that were recently accreted. The mean infall time of the galaxies is typicall $2.7^{+1.4}_{-1.7}$, $4.5^{+1.9}_{-2.2}$, and $5.1^{+1.8}_{-2.1}$ Gyr for the recent, intermediate, and early infall zones, respectively. This is based on the comparison with the cluster simulation at z = 0 in Pasqualiet al. (2019). (However, we also note that there is

 $[\]overline{^{21}}$ While the original definition of Noble et al. (2013) is based on \mathfrak{g}_{00} for a cluster radius, we note that usinggoinstead makes only a 0.15 dex shift in our the projected phase space to divide galaxies into different infall time proxy (i.e., $log[(r_{pro}/r_{500}) \times (|\Delta v|/\sigma_{cl})]$) and thus does not the projected phase space to divide galaxies into different infall qualitatively change our results given r_{500} ; 0.7r $_{200}$ (e.g., Ettori & time stages for a z ~ 0.9 cluster. Their analysis and later studiesalestra 2009).

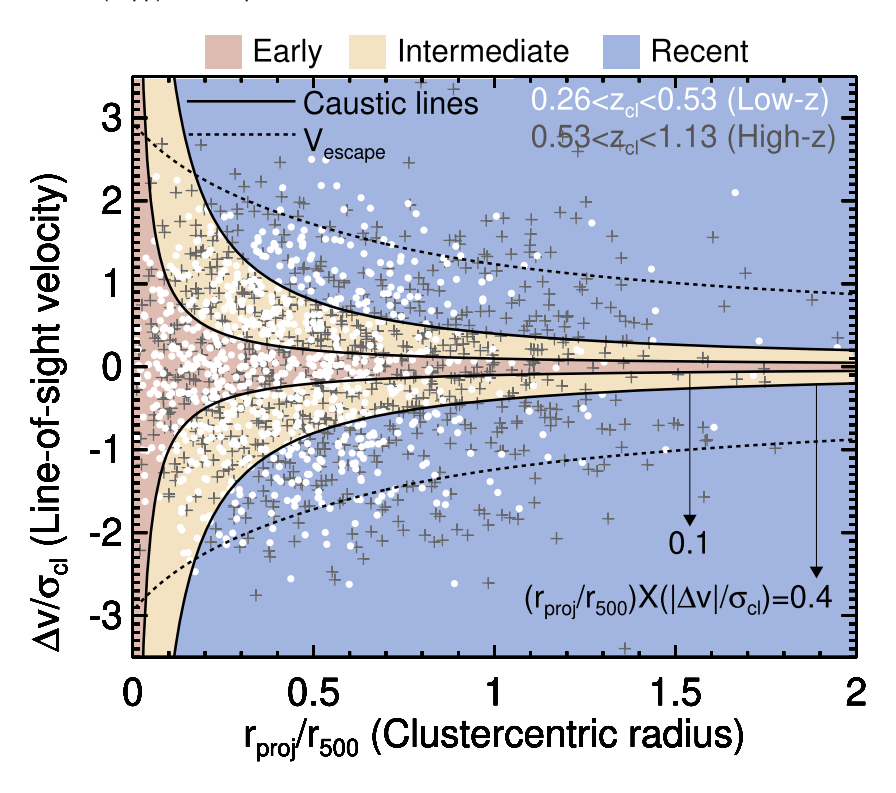


Figure 3. Projected phase space diagram of galaxies stacked from 105 clusters at 0.26 < z < 1.16h (£.eqrmalized line-of-sight peculiar velocity vsrojected clustercentric radius) which shows a variety of accretion stages of cluster galaxies since infall he white circles and gray plus signs indicate the low-redshift (0.26 < z < 0.53) and high-redshift (0.53 < z < 1.13) subsample galaxies pectively. The phase space is color coded by different infall time zones based on the caustic lines (i.e., solid lines; Section 3.2): early infall (reft) or $(1.50)^{1/3} = 1.00$ or $(1.50)^{1/3} = 1.00$

scatter in the mean infall time space due to projection effects

For the projected phase spac σ_{cl} are based on the spectroscol (Section 2.3).In particular, the line of-sight peculiar velocity (Δv) is expressed as follows:

$$DV = C' \left(\frac{Z_{gl}}{1 + \frac{Z_{cl}}{C_{cl}}}\right), \qquad (5)$$

where ζ_{l} , z_{cl} , and c are the redsh and the speed of light, respective ly. The r_{proj} is derived by measuring the angulaseparation and a galaxy's projected location obtain the clustercentric radius ζ_{l} , we derive the ζ_{l} 0 of our sample clusters using the clusters using the clusters using a spherical mass density profile,

$$M_{500} = \frac{4p}{3} r_{500}^3 50 r_{\text{crit}}, \tag{6}$$

where ρ_{rit} is the critical density of the Universe at the cluster

We select galaxies with $|\Delta v|/\omega$: 3.5 and r_{proj}/r_{500} < 3 as infalling cluster galaxies as state 1 in Section 3.1. Figure 3 shows the projected phase space of the sample galaxies. Galaxies mostly populate region: within $|\Delta v|/\sigma|_{cl} \square$ 2 and

pro√r $_{500}$ □ 1.5.These regions are closely matched with the nner region of the escape velocity radial profile (dashed lines) If the median mass (4.97 × 10 $^{\circ}$ M_e) of our sample clusters. Shis suggeststhat the bulk of infalling galaxies are gravitationally bound by cluster potential wells. To derive the escape velocity profile, we assume a Navarro–Frenk–White (NFW) dark matter halo density profile (Navarro ætl. 1996) and a cluster concentration parameter of 4.

The early and intermediate infall zones are all located within the inner region of the escape velocity profile, while the recent infall zone spans the escape velocity profile. The comparison of infall zones with the escape velocity profile makes intuitive sense in that galaxies thathave infallen at earlier times are expected to have virialized earlier than those that have infallen more recently. Our low-z (0.26 < z < 0.53) and high-z (0.53 < z < 1.13) subsamples(i.e., gray and white points, respectively, in Figure 3) show similar phase space distributions.

4. Results and Discussion

In this section, we look at how the mean age of the galaxies (using D_n4000) statistically varies with their infall time proxy to investigate the environmental quenching effects since the galaxies entered into clusters. In Section 4.1, we show the trends of D_n4000 with infall time proxy across redshifts z = 0.26-1.13. In Section 4.2, we investigate the galaxy

luminosity dependence(using L_i/L^{*}) of the environmental quenching by dividing galaxies into "faint" (sub-L/L < 1) and "bright" (super-L, L/L > 1) galaxies. In Section 4.3, we simultaneously controfor the galaxy luminosity and redshift dependences of the environmental quenching by dividing galaxies into redshift and luminosity bins. We discuss the potential projection effects in our projected phase space analysis in Section 4.4.

4.1. Quenching since Infall: A Continuous 40000 Increase of Galaxies from Recent to Early Infall

We now investigate how the Q4000 (mean stellar age) of galaxies varies with time since infall to study the environmental impacts on the star formation of galaxies. Figure 4 shows D_n4000 versus $(f_{roj}/r_{500}) \times (\Delta v/\sigma_{cl})$ (a proxy for infall time; see Section 3.2 for details). The top panel shows the distribution of galaxies atall redshifts (0.26 < z < 1.13)The colored diamonds indicate the mean 4000 of galaxies in the corresponding colored infall time zone, hich is derived from 1000 bootstrap realizations accounting for the D_n4000 uncertainties.

Notably, there is a continuous increase in the mea# 1000 of galaxies with the infall time proxy moving from recentto early infall populations. The increase in the mean \$\textstyle{Q}4000 is from 1.51 \pm 0.01 to 1.62 \pm 0.01The net increase (Δ D4000) corresponds to an age increase of ~0.71 ± 0.4 Gyr based on a simple stellar population modeling assuming an instantaneous burst of star formation with solar metallicity from Kauffmann et al. (2003)²² The quantitative age increase estimated above only describes the relative difference in mean stellar age between recentand early infall populations. This average age difference is estimated from galaxies that span a wide range of redshifts (0.26 < z < 1.13)therefore the reported age difference does not apture any redshift-dependeage differences between infall zones. We examine in detail the redshift dependence of the age difference between infall zones in Section 4.3.

The continuous increase in the mean \$\textstyle{L}4000 of galaxies with infall proxy is also shown by the gradual shift of the D_n4000 histograms of each infalkone in the right panels of Figure 4. That is, early infall galaxies (red solid line) tend to have a larger fraction of high_r **2**000 (D₁4000 □ 1.5) galaxies compared to the receninfall counterparts (blue dashed line), and the intermediateinfall galaxies show the intermediate distribution between recent and early infall zoneshis steady shift of the distributions toward larger D4000 strength from recent (blue) to early (red) infall populations suggests that the mean age of cluster galaxies increases with time since infall, although there is a broad distribution of 40000 values in each infall zone, which is reflected in the overlapping D_n4000 histograms of different infall populations.

The different D_n4000 distributions between different fall time zones are further supported by the two-sample Kolmogorov-Smirnov (K-S) test (Table 2). Table 2 presents the results of the K-S tests for the null (i.e., false-positive)

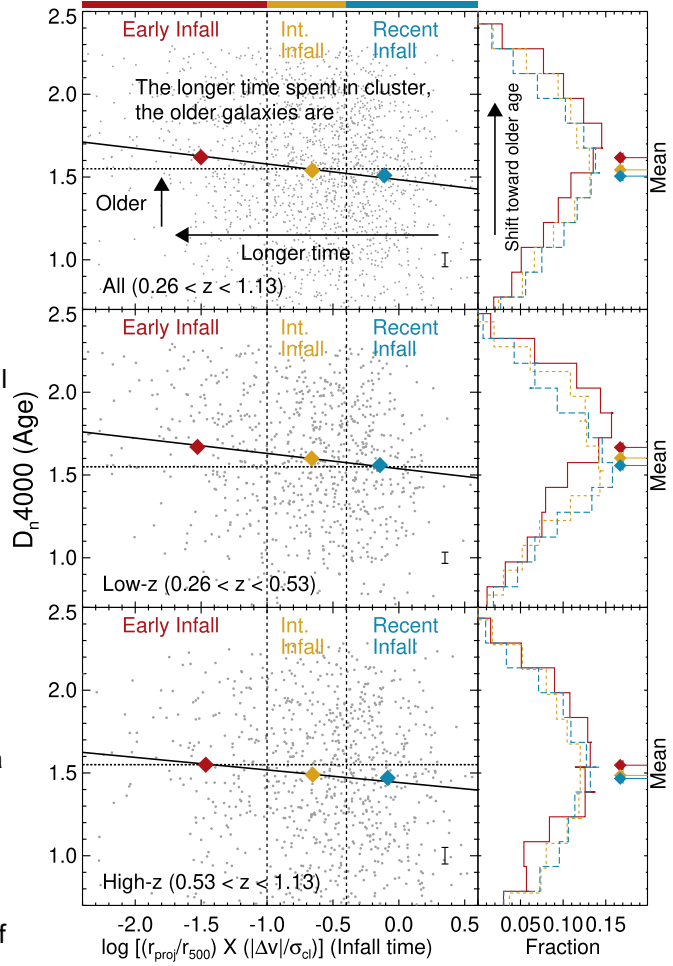


Figure 4. Diagram showing that galaxies that have infallen at earlier times are quenched earlier across all of our sample redshifts (z = 0.26-1.13). The 4000 Å break (D₁4000) and the position in the projected phase space_D((fr 500) × $(\Delta v/\sigma_{cl})$; Figure 3) are used as proxies for mean stellar age and cluster infall time, respectively. In each panel different colors indicate different infall time zones separated by vertical dashed lines and the color bars on top (Section 3.2): early (red), intermediate (orange), and recent (blue) infall. Top: distribution of galaxies at all redshifts (0.26 < z < 1.13). Colored diamonds indicate the bootstrapped mean, 2000 of galaxies in the corresponding infall time zones. The error of the mean is smaller than the symbol size. The black solid line is a linear fit to individual galaxies derived from bootstrapping with the \$\mathbb{A}000\$ uncertaintiesaccounted for (Table 3). The dotted horizontal line indicates $D_{\rm p}4000 = 1.55$ as the guideline used in the literature to separate star-forming $(D_n4000 < 1.55)$ and quiescent $(D_n4000 > 1.55)$ galaxies. The typical uncertainty of D₁4000 is marked in the bottom rightof each panel Middle: distribution of low-redshift (0.26 < z < 0.53) subsamples. Bottom: distribution of high-redshift (0.53 < z < 1.13) subsamples. Note that there is a continuous increase in the mean D4000 of galaxies with the infall time proxy at all redshifts (from top to bottom), as also shown in the histograms on the right. The continuous D4000 increase with the infall time proxy (from recent to early infall) shown in all panels suggests that alaxies become quenched as they spend a longer time in the cluster environment at all redshifts z = 0.26-1.13 (Section 4.1).

probability that the two selected distributions are statistically different. The left column of the table shows that D₀4000 distributions between early infallers and the other two

We also perform a linear fit to the \$\mathbb{D}\$000 versus infall time proxy relation for galaxies with the following form:

$$D_r 4000 = a \log[(r_{proj}/r_{500}) \cdot D(V/s_{cl})] + b,$$
 (7)

The "exact" net age increase depends on the details of the assumed stellar categories of infallers are statistically different, with null population modeling parameters, such as the shape of the star formation historprobabilities of <0.05. and metallicity (seep.g., Figure 2 of Kauffmann etal. 2003 and Figure 1 of Hernán-Caballero etal. 2013). For instance,the variations in the assumed metallicity (0.4–2.5 χ) result in the corresponding age increase to t increase to vary from ~0.31 to ~1.12 Gyr. However, more importantly, we note that there is no qualitative change in our interpretation of the D_n4000 increase as the age increase of galaxies with infall time proxy.

Table 2 The Two-sample K-S Test Shows whether the 4000 Distributions of Different Infall Time Zones Are Statistically Different (Section 4.1 and the Right Panel of Figure 4)^{a,b,c}

	Total-z (0.26 < z < 1.13)	Low-z (0.26 < z < 0.53)	High-z (0.53 < z < 1.13)
Early-intermediate	0.002	0.03	0.3
Early-recent	0.00004	0.0007	0.07
Intermediate-recent	0.3	0.4	0.8

where α and β are the slope and intercept of the relation. respectively. We perform 1000 iterations for the fits by accounting for the D_n4000 uncertainties We find a negative slope (α) of -0.096 ± 0.016 of the relation that is constrained to be negative at high statistical significance. This suggests the the D_n4000 of galaxies increases with lower (r_{proi}/r₅₀₀) × $(\Delta v/\sigma_{cl})$, meaning older age with longer time spent in clusters since infall. We note, howeverthat the quantitative slope that we measure could be subjetto small selection biases due to our observational selection effects, specifically that we preferentially target red-sequence(passive) galaxies (see Section 3.1 for details).

The middle panel of Figure 4 shows the distribution of lowredshift (0.26 < z < 0.53) subsamples. The low-z galaxies show similar trends as those of the entire sample (top panel). That is Notes. they also show a constant increase of 000 with infall proxy, with a fitting slope (α) of -0.093 ± 0.020 (Table 3) and statistically different D_n4000 distributions between early infallers and other infallers by the K-S test(middle panel of Table 2). A noticeable difference from the entire sample is that into faint (sub-L*, L_i/L* <1) and bright (super-L*, L_i/L* >1) subsamples the D_04000 of low-z galaxies ison averagelarger by ~0.05, regardless of infalltime proxy. This is further shown by the larger interceptvalue of the fitted D₁4000 versus infallproxy relation in low-z subsamples compared to the entire sample in Table 3 (i.e., 1.54 ± 0.02 versus 1.48 ± 0.01 for low-z subsamples and the entire sample, respectively). The $\Delta D_n 4000$ of the mean $\Omega 4000$ from recent to early infall is a 0.11 increase from ~1.56, which corresponds to an ~0.84 ± 0.6 Gyr age increase.

redshift (0.53 < z < 1.13) subsamples.Like the other two redshift bins (top and middle panels), the high-z subsamples also show the increasing \$\textstyle{2}4000 trends with infall proxy, as shown by the increasing mean 40000 and the gradual shift of the D_n4000 histogram toward largerD_n4000 strength when moving from recent to early infallers. We also found a negative the D_04000 versus infall proxy relation compared to the entire slope (α of -0.078 ± 0.025) of the relation for high-z galaxies, sample and low-z subsamples in Table 3. which is slightly shallower but still consistentwith the other redshift bins within 1σ uncertainties (Table 3).

The K-S test for the Q4000 distributions of different infall zones of the high-z subsamplesdoes not show statistical significance, as the related null probability that the tested 0.05 (right column of Table 2). Nonethelesslike the other redshift bins, the null probabilities systematically vary with infall time zones, such that we see the same qualitative trends in D_n4000 with infall time proxy. These systematic K-S test

Table 3 The Fit Relation of D₄4000 vs.Infall Time Proxy Shows the Consistent Negative Slope α across All Redshift and Luminosity Bins (Sections 4.1–4.3)

Redshift/Luminosity ^c	Slope d ^d	Intercept β ⁱ
atotal-z /faint+bright	-0.096 ± 0.016	1.48 ± 0.01
Low-z/faint+bright High-z/faint+bright	-0.093 ± 0.020 -0.078 ± 0.025	1.54 ± 0.02 1.44 ± 0.02
Total-z /faint	-0.082 ± 0.022	1.45 ± 0.02
Low-z/faint	-0.082 ± 0.022 -0.080 ± 0.027	1.52 ± 0.02
High-z/faint	-0.052 ± 0.035	1.39 ± 0.03
Total-z/bright	-0.108 ± 0.024	1.53 ± 0.02
Low-z/bright	-0.096 ± 0.033	1.60 ± 0.04
High-z/bright	-0.095 ± 0.033	1.50 ± 0.03

results with infall zones at least suggest that the D_n4000 distribution of our high-z subsamples is related to the galaxies' infall time proxy. The $\Delta D_n 4000$ of the mean $D_n 4000$ from recentto early infall for high-z galaxies is an ~0.08 increase The bottom panel of Figure 4 shows the distribution of high- from \sim 1.47, which corresponds to an \sim 0.63 \pm 0.4 Gyr age increase.

> Contrary to the low-z galaxies, the high-z subsamples show, on averagesmaller D₁4000 values by ~0.05 compared to the entire sample at all infall proxies. The smaller 4000 value of the high-z subsamples is also seen by their smallerceptof

This redshift dependence of the D_n4000 strengthsacross infall proxies is likely attributed to the redshift evolution of the star-forming main sequence such that the average D₁4000 strength of galaxies at fixed stellar mass decreases with increasing redshift(e.g., Whitaker et al. 2012; Haines et al. distributions are drawn from the same distribution is larger than 2017; Pandya et al. 2017). We will further discuss the redshift dependence of the \$\mathbb{P}\$000 distributions of our sample galaxies associated with infall time in Section 4.3.

> The continuous galaxy age (D4000) increase with infall time proxy (Figure 4) is also consistent with the increasing

^a Galaxies are classified as earlintermediateand recent infall galaxies based on their location in the phase space as a proxy for their infall stage into the cluster (Figure 3 and Section 3.2).

b Numbers indicate the null (i.e., false-positive) probability that a given pair of infall time zones' (early, intermediate, an 400 mis bibutions are drawn from the same parent distribution.

c Bold null probabilities indicate that the 🖾 000 distributions of a given pair of infall time zones are statistically differemaing less than 0.05.

^a The relation is described by 4 000 = α log [(r_{proj}/r_{500}) × ($\Delta v/\sigma_{cl}$)] + β , same as Equation (7).

Total-z, 0.26 < z < 1.13; low-z, 0.26 < z < 0.53; high-z, 0.53 < z < 1.13.

 $^{^{\}rm c}$ Galaxy i-band luminosity (\mathbb{/}L^*) is used (Section 2.2). Galaxies are divided

relative to the characteristic luminosity * L d The values and uncertainties are derived from 1000 bootstrappings of the fit with the D_n4000 uncertainties accounted for.

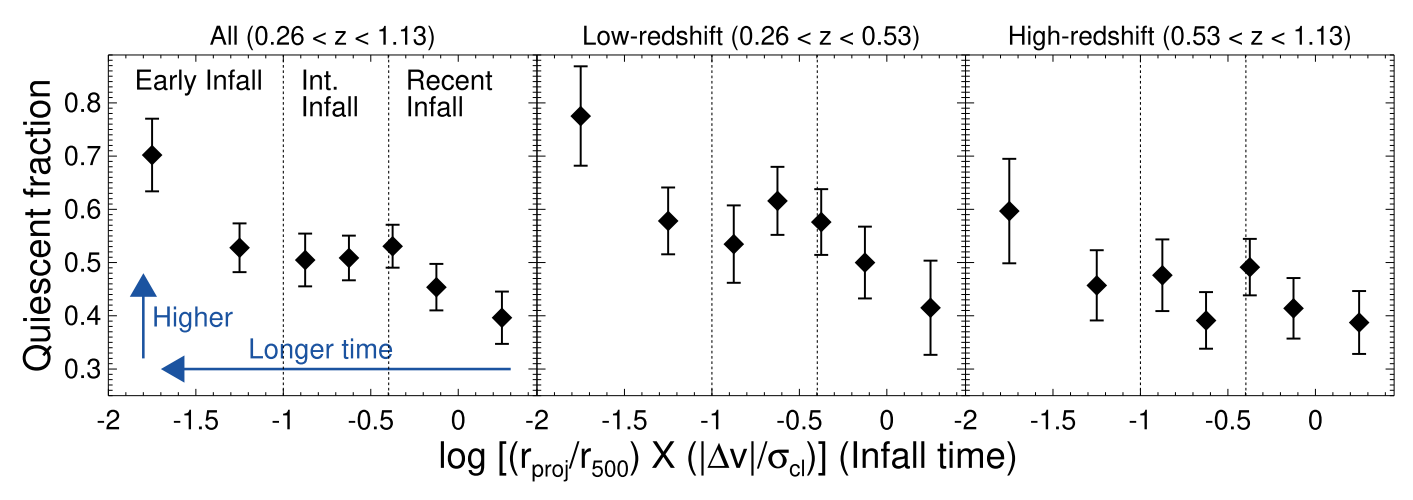


Figure 5. Diagram showing that the fraction of quiescent galaxies)(increases with infall time proxyEach panel shows the same relationship but different redshift ranges, as indicated on the tops of the panels. Quiescent galaxies are defineedas D.55. The fo are calculated in bins of 0.25 or 0.5 dex (smaller bin size adopted for crowded infall bins) of infall proxyldg[(r_{proj}/r_{500}) \dot{D} V/S_{cl})). The error bars indicate 1σ uncertainties based on Poisson statistics is an increasing f with infall proxy in all panels (i.e., regardless of redshift), although the low-z galaxies (middle panel) show a systematically log imparted to the high-z galaxies (right panel) for any given infall bin (see Section 4.3 for the redshift dependence of environmental quenching trends). The increasing quiescent frac of galaxies with infall time proxy suggests that galaxies become quiescent due to longer exposure to environmental effects.

fraction of quiescentalaxies (f) with infall proxy shown in Figure 5. In the figure, f_{O} is calculated as the fraction of galaxies whose D_n4000 is >1.55 in bins of infall proxy. Indeed, the f_Q increases from 0.4 \pm 0.05 to 0.7 \pm 0.07 while moving from recent to early infall zones across alredshifts (z = 0.26-1.13).

These steady increases in \$\mathcal{P}\$000 and fo with infall time proxy would suggest that galaxies that have infallen into environmental effects. Our findings are qualitatively consistent stripping since infall (Jung et al2018). with previous studies for several high-z ($z \sim 1$; Noble et al. 2013, 2016; Werner et al. 2022) and local (z < 0.2) clusters (Pasquali et al. 2019; Smith et al. 2019; Upadhyay et al. 2021), considering the similar mass range (and thus gravitational as well as recent cluster simulations showing systematic suppression of star formation of galaxies since infaWetzel et al. 2013; Oman & Hudson 2016; Rhee et al. 2020; Coenda et al. 2022; Oman et al. 2021). Our time-averaged kinematic analysis spans a wide range of redshift = 0.26-1.13 with a sample of clusters that are uniformly selected above an approximately constant mass threshold. and reveals a remarkably consistent picture of environmental quenching extending out to $z \sim 1$.

For instance, environmental mechanisms such as ram pressure stripping (Gunn & Gott 1972; Abadi et al. 1999; Ebeling et al. 2014), starvation (Larson et al. 1980), harassment A slow quenching process, such as the gradual shutoff of gas (Moore et al. 1996), and tidal interactions(Byrd & Valtonen 1990) have been suggested as the ones enabling suppression of star formation of galaxies in cluster and eed, a systematic gas stripping process has been observed in the Virgo and A963 clusters based on the projected phase space analysis (Vollmer et al2001; Boselli et al.2014b; Jaffé et al. 2015; Yoon et al. 2017; Morokuma-Matsui et al. 2021), where medium gas A slow starvation quenching process would take the level of HI gas stripping is closely related to the infalling stages identified in the phase space (see, e.g., Figure 5 of Yooa galaxy has fallen into the galaxy cluster environment, which

galaxies, such as warm dust (Noble et al. 2016), molecular gas (CO; Fumagalli et al. 2009; Boselli et al. 2014a; Lee & Chung 2018) and dust (Cortese et a 2016; Longobardi et al. 2020), is also reported in cluster environments. hese results clearly show that gas stripping is actively occurring in cluster galaxies (likely) through the ram pressure by the hot ICM in the deep gravitational potential well of clusters. This is further supported by the recentcosmological cluster simulation that clusters earlier are guenched earlier due to longer exposure to shows the systematic gas depletion of galaxies by ram pressure

> It is not unreasonable to expect that such ram pressure stripping has occurred in our sample cluster galaxies as well, potentialwell) of our sample clusters with those reported for gas stripping (i.e., $1-8 \times 10^{-14} \text{ M}_{\odot}$). Indeed, the significant X-ray detection (X-ray luminosity > 10^{44} erg \bar{s}^1) and the associated hot ICM temperature (>2 ×71KI) are found in our cluster subsamples across all redshifts (McDonald e2a1.4; Bulbul et al. 2019). However, ram pressure stripping should be most effective on low-mass systems (e.g., Janz et al. 2021), and the luminosity cut of our analysis (i.e., L_i/L Section 3) restricts our sample to moderately massive galaxies, suggesting that we should not be highly sensitive to the effects of the ram pressure mechanism.

supply ("starvation"; see, for example, Larson et al. 1980), seems to be a plausible quenching process driving the gradual age (D_n4000) trend with infall proxy in our sample galaxies (Figure 4). Physically, this process is one that acts via the truncation of the galaxy's circumgalactic medium, rather than a faster mechanism that achieves the rapid removal of interstellar effect over the course of several dynamical crossing times after et al. 2017). Furthermore, the stripping of other components of is in good agreement with our measurement of a small average net age increase from recentlo early infall populations (i.e., 0.71 ± 0.4 Gyr) compared to the typical dynamical timescales

> A slow quenching trend is also consistent with the approximately constantslope (α) that we measure for the

We note that our results of increasing D₁4000 with infall time proxy virtually do not change even when the sample clusters are divided into specific of 1–3 Gyr of cluster galaxies (e.gRhee et al.2020). cluster mass criteria (e.g., the expected mass-growth curve with redshift; Fakhouri et al. 2010) within the sample clusters' mass range, 3 × 10¹⁴ $M_e \ \square \ M_{500} \ \square \ 3 \times 10^5 \ M_e$ (Section 2.1).

mean stellar population age versus infall proxy relation (i.e., the Dependence of environmental quenching on galaxy luminosity

 $D_n4000 \text{ versus } \alpha \log \left[(r_{pro}/r_{500}) \times (\Delta v/\sigma_{cl}) \right] + \beta \text{ relation};$ Equation (7)). Specifically, the slope α does not significantly depend on the galaxies 'L_i/L * (stellar mass), as both bright $(L_i/L^* > 1)$ and and faint $(L_i/L^* < 1)$ subsampleshave statistically similar α (~-0.09) at all redshifts (Table 3).The similar α we measure across galaxy luminosity suggests that the environmental quenching mechanism acting on these galaxies is not strongly dependent on either galaxy stellar mass or orbital velocity, which matches the expectation for the starvation effect in cluster environments. Qualitatively, our results are in broad agreement with the known "delayed-thenrapid" quenching processes (e.dWetzel et al. 2013; Haines et al. 2015; Gallazzi et al 2021).

We also note that while the averagenet age increase (0.7 ± 0.4 Gyr) seen in our sample galaxiesappearsto be broadly consistent with the quenching age (0.1-1.3 Gyr) by the ram pressure gas stripping in localalaxy clusters (Crowl& Kenney 2008; Boselli et al. 2016), one should be cautious in directly comparing the age increasewe measurewith the quenching ages from the literature. This is due to the differenceuminosity dependence of the environmental quenching effect (i.e., the in how the quenching-related ages are measured between the continuousage (D_n4000) increase of galaxies since infall). The diamonds studies such that our measurement is based on the average neand associated error bars are the bootstrapped mealoon strength and the age increase of stellar populations since infall, whereas the SF the different i-band luminosity bins: all (black), faint (sub-L; orange), and quenching age often measured in the literature is considered to right (super-L, blue). Note that both the faint and bright subsamples show a be the time taken for a galaxy to transform from gas-rich and star-forming to a totally quenched passive system.

that are likely at play in our sample galaxies. Of them, preprocessing—i.epre-exposure of group-scale environmental effects before infalling to the main cluster(Balogh et al. 2000; Fujita 2004; Han et al. 2018; Lee et al. 2022)—is known to be able to quench the starformation of infalling galaxies even in the clusteroutskirts ($\square R_r$; Balogh et al. 2000), the region where cluster environmenteffects are expected to be insignificant. Indeed, recent observations for high-redshift clusters (z ~ 1) suggesthat the majority of massive galaxies are quenched during infall in the cluster outskirts $(1 < R/R_{200} < 3)$, which might imply preprocessing effects prior to infall (Werner et al.2022).

While our analysis alone cannobin down the most likely environmentalmechanisms responsible fothe quenching of cluster galaxies, we emphasize that the stead 000 increase with infall proxy in Figure 4 strongly indicates the environmental quenching atplay over a wide span of redshift(0.26 < z < 1.13). Also, our results are qualitatively consistent with recent work at similar redshifts (0.3 < z < 1.5; Webb et al.2020; Khullar et al. 2021), where the authors used a stellar population fitting analysis to measure the star formation histories and ages of quiescent cluster galaxies.

4.2. Luminosity Dependence of Environmental Quenching: Trends with Faint ($L/L^* < 1$) and Bright ($L/L^* > 1$) Galaxies

In the previous section, we have shown that there is a continuous increase of \$\overline{\pi}4000\$ with infall time proxy, which suggests that alaxies that have infalled earlier are guenched earlier due to environmental effects. In this section, we investigate a galaxy luminosity dependence of the environmental quenching trend. We divide our sample galaxies into faint (sub-L; L_i/L < 1) and bright (super-L; L_i/L subsamples based on their i-band luminosity (Section 2.2).

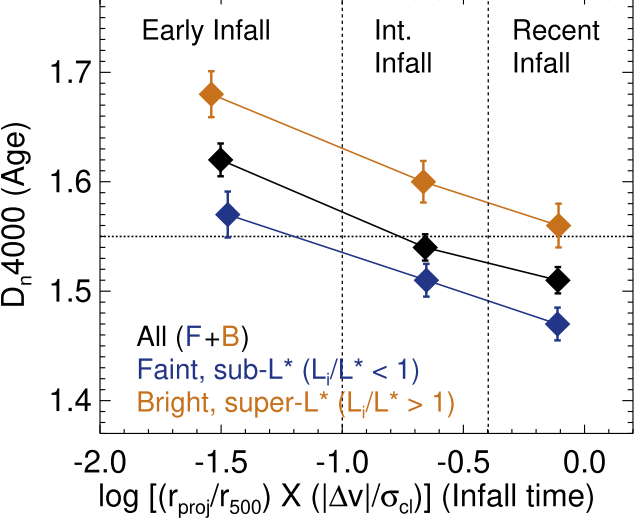


Figure 6. Similar to the top panel of Figure 4 but focusing on the galaxy continuous D₁4000 increase with infall proxy. However, at all fixed infall zones, bright galaxies have larger mean D_n4000 compared to their faint We also note that there are other environmental mechanism segardless of the galaxies' luminosityet the exact age (\$\text{L}4000\$) depends on the galaxies' luminosity due to an internathass quenching (i.e.downsizing) effect at a fixed environment (Section 4.2).

Figure 6 shows the same \$\textstyle{1}\text{4000 versus infalltime proxy} diagram as the top panel of Figure 4 but focusing on the galaxy luminosity dependence by splitting it into faint and bright subsamplesThe black diamonds and associated error bars are the bootstrapped mean 2000 strength and the 1σ spread of the full sample, same as in the top paneof Figure 4. Orange and blue indicate the same symbols as black but for faint and bright subsamples espectively.

Notably, both the faint and bright subsamples qualitatively show the same environmental quenching trend with infall time, as both subpopulations show the continuous increase of D_n4000 with the infall time proxy. The faint and bright subsamples also have slopes (α) Q#D00 versus infall proxy relation consistent within 1σ , with $\alpha = -0.082 \pm 0.022$ and -0.108 ± 0.024 for faint and bright galaxies, respectively, as in Table 3. This means that the environmental quenching affects galaxies regardless of galaxy luminosity (stellar mass).

However, there is a noticeable difference between the faint and bright subsamples, such that the bright subsamples always have a larger mean \$\mathbb{Q}4000\$ strength than their fainbounterparts across infallzones. This trend does notarise from any potential dependence of luminosity on infall proxy in the sense that bright galaxies might be preferentially located toward earlier infall zones and thus have a larger mean 40000 than

Note that while the i-band luminosity (L/L *) is a useful quantity for the optical light of stellar populations, it is only a rough proxy for stellar mass and subject to significant mass-to-light (M/L) ratio variations. This caveat especially applies forgalaxies at high redshift (z > 0.8), where the i-band samples rest-frame light blueward of the 4000 Å breahly a small fraction (8%) of our galaxies are at z > 0.8, so that the large majority of our analysis is based on galaxies where the i-band samples rest-frame lightward of the 4000 Å break.

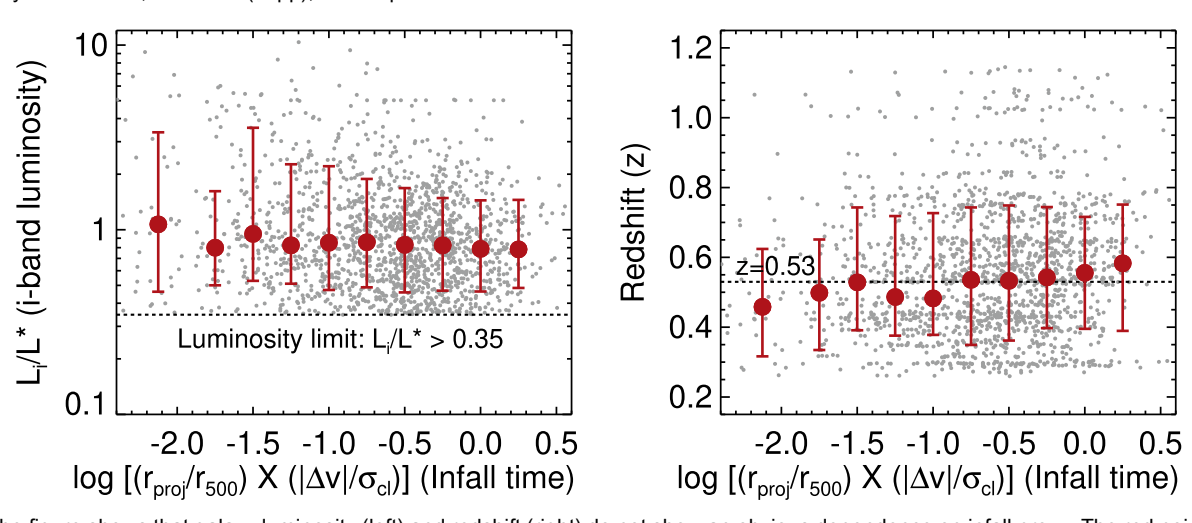
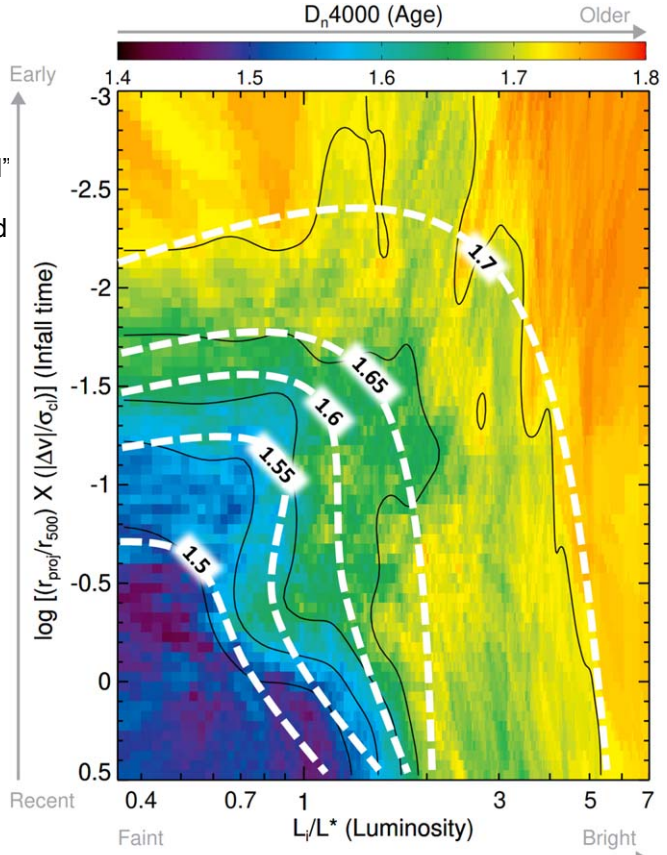


Figure 7. The figure shows that galaxy luminosity (left) and redshift (right) do not show an obvious dependence on infall proxy. The red points with error bars indicated the median values and associated 1σ spread per infall proxy bin. In the left panel, the galaxy luminosity infall proxies, although the median redshift seems to slig decrease with infall proxy within 1σ. In the right panel, the redshift distribution is also consistent across all infall proxies, although the median redshift seems to slig decrease with infall proxy within 1σ population spread. Little (or no) dependence of luminosity and redshift on infall proxy suggests that the interproxy with infall time proxy (e.g., Figure 4 and Section 4.1) is not driven by either luminosity or redshift. Rather, it is most likely due to environmental quenching such that galaxies that have infallen earlier stopped star formation earlier. It is also regardless of specific galaxy luminosity (Figures 6 and 8 and Section 4.2) and redshift bir (Figure 9 and Section 4.3).

the faint counterparts. We show that the luminosity distribution of sample galaxies is similar across all infall proxies in the left panel of Figure 7.

Thus, at a fixed infall zone (environmentaleffect), this quantitative D_n4000 difference between faint and bright subsamples is likely attributed to the mass-dependent "internal" quenching of galaxies (e.g., Gavazzi & Scodeggio 1996; Boselli et al. 2001; Peng et al. 2010; Kim et al. 2016, 2018, and referencestherein). That is, more massive (bright) galaxies become quenched earlier than their less massive (faint) counterparts. This mass quenching may be attributed to mechanisms such as viriashock heating of infalling gas in massive galaxy halos (e.g.pekel & Birnboim 2006) and/or secular AGN feedback from the supermassive black holes in the galaxy center (e.gChoi et al. 2015; Bluck et al. 2022).

The individual effects of environment-related infalltime proxy and galaxy luminosity (L) on quenching as traced by mean galaxy age are demonstrated in Figure 8 is generated by creating a density map of the spatially averaged D_n4000 value within a grid of infall proxy and luminosity. Each pixelated grid position is 0.025 in L_i/L^{*} by 0.05 in $\log[(r_{\mathrm{proj}}/r_{500})$ ' D($V/s_{\mathrm{cl}})$], and within each grid pixel, we measure the mean 2000 strength of the neares 100 sample galaxies. Due to some regions of the grid space being very sparsely sampledwe then apply a 2D Gaussian smoothing kernel with a width of 3 grid pixels to improve the visualization of the resulting density map. Clearly, the mean ODO (age) of the galaxies is a function of both environment and luminosity, as the colored D_n4000 strength continuously increases with infall proxy (y-axis) and luminosity (x-axis) However, when fixing one parameter (i.e., x- or y-axis), the mean D_n4000 strength increases along with the other parameteris means that a continuous \$\mathbb{A}000\$ increase along with the y-axis (infall proxy) is due to the environmental quenching effectat any given luminosity. This trend is also consistent with the "knee"shaped white dashed lines thatare the contours of constant D_n4000 strengthstracing the mean D_n4000 distributions of sample galaxies.



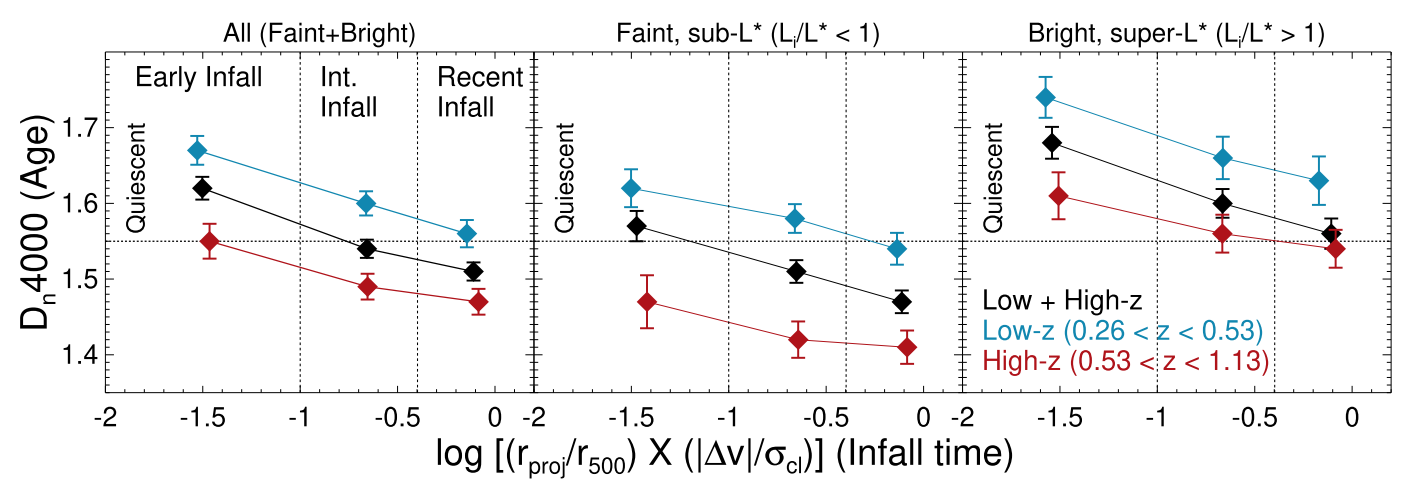


Figure 9. Diagram showing the trends of quenching since infall (i.e., a continuous increase of Moth infall time proxy) across redshift and luminosity bins. In all panels, different colors indicate different redshift bins: black, all z (0.26 < z < 1.13); blue, low-z (0.26 < z < 0.53); and red, high-z (0.53 < z < 1.13). Different panels show differentluminosity bins: left, all (faint+bright); middle, faint (sub-L; L_i/L * < 1); and right, bright (super-L; L_i/L * > 1). The diamonds with error bars indicate the bootstrapped mean \$\textit{2000} and associated standard deviation of sample galaxies in each iza \$\textit{1200} also accounts for \$\textit{14000}\$ measurement uncertainties. The formats are the same as in Figure 4. By comparing the blue and red points in each panel, it is clearly shown that low-z galaxies have a larger me Dn4000 than their high-z counterparts at a fixed infall zone (fixed environmental effect), regardless of luminosity. This is due to the redshift dependence of the starforming main sequence (Section 4.3). Also, by comparing the middle and right panels for the same colored points, it is shown that bright galaxies have a larger me Dn4000 than their faint counterparts at a fixed infall zone across redshift, which is due to the mass-dependent quenching effect (Section 4.2). Thus, by dividing san galaxies into specific redshift and luminosity bins, this figure clearly shows that environmental quenching does exist and impact galaxies since their infall into cluste at all redshifts and luminosities et the exact age (\$\text{\$\text{\$\pi\$}}4000) depends on both redshift and luminosity at a fixed environment (infall zone; Section 4.3).

Therefore, Figures 6 and 8 suggest that environmental quenching impacts galaxies independent of galaxy luminosity, decreasewith decreasing redshift, the D_n4000 strength of although the exact age (D_n4000) dependson the galaxies' kinematic environmental results through infall time proxy show potential dependence of galaxy redshigh infall proxy in the two main drivers of galaxy quenching (e.g.,eng et al.2010; Smith et al. 2012; Kawinwanichakijet al. 2017; Sobralet al. 2022).

4.3. Environmental Quenching Observed across Wide Ranges 1σ population spread (i.eΔz ~ 0.1 across infall proxies). of Redshift (0.26 < z < 1.13) and Luminosity $(0.35 < L/L^* < 10)$

occurs since infall such that the galaxies 4000 continuously increases when moving from recent to early infallers (Figure 4)subsamplesshow an environmental quenching effect (a Also, environmental quenching seems to impact galaxies regardlessof their luminosity (Figures 6 and 8). We now control for redshift and luminosity simultaneously to further isolate environmentalquenching effects, as both parameters can independently alter the 19000 strengths (similarly sSFR) of the galaxies regardlessof environment(e.g., Kauffmann et al. 2003; Haines et al2017; Kim et al. 2018).

Figure 9 shows the same D₁4000 trends with infall time proxy as in other figures but further divided by specific redshift independent of specific redshift bins. and luminosity bins.

First, in all panels showing different luminosity binsow-z galaxies (blue points) clearly show larger mear 1000 values than their high-z counterparts (red points) across in fadines. At the same time, both redshift bins show a continuous increasecross allredshift and luminosity bins. This is also supported of mean D₁4000 with infall time proxy due to the environmental quenching atplay at all redshift bins. This systematic redshift dependence of D_n4000 at a fixed infall proxy (environmentaleffect) and luminosity is likely attributed to (e.g., Whitaker et al. 2012; Sobral et al. 2014; Pandya etal.

2017). As the sSFRs of galaxies for a given stellar mass galaxies given luminosity is also expected to increase with luminosity due to the internal mass quenching mechanism. Oudecreasing redshift. Note that this trend does not arise from any a consistent picture, where stellar mass and environment are tisense that low-z galaxies might be preferentially located toward earlier infall zones and thus have a larger mean 40000 than their high-z counterpartsThis is shown in the right panel of Figure 7, where the redshift distribution of sample galaxies is mostly similar across all infall proxies, although the median redshift appears to slightly increase with infall proxy within a

Also, by fixing the redshift bins (i.e. focusing on the same colored points across panels), is clear that bright (super-L) So far, we have demonstrated that environmental quenchinggalaxies have larger mean \$\int_0000\$ values than the fain(sub-L*) galaxies at all infall zones, while both luminosity continuous increase of D_n4000 with infall time proxy). As noted in Section 4.2, this luminosity dependence of D00 is likely explained by the mass quenching effectin that more massive (bright) galaxies tend to stop star formation earlier than those with less mass (fainte.g., Peng et al. 2010; Kim et al. 2016, 2018; Haines et al. 2017). By splitting into low- and high-redshift bins, we further show that this luminosity dependence of D_n4000 at a fixed infall proxy exists

The trends shown in Figure 9 further suggest that environmentalquenching indeed affects galaxies since infall regardless of redshiftand luminosity, as clearly shown by the systematic increase of the mean 4000 with infall time proxy by the similar gradient (slope α) of P000 versus infall proxy relation for all subsamples (Table 3) that are consistent within the uncertainties. However, it is also evident that the exact D_n4000 strength (age) at a fixed environmental effect shows the the redshift-dependent star-forming main sequence of galaxiessystematic dependency on redshift and luminosity due to their individual effects on Q4000 as discussed above.

4.4. Caveats on Projected Phase Space

Despite the exceptional usefulness of the projected phase space for investigating environmenteffects.it is also worth noting that there is a spread in our infall time proxy due to sources of uncertainty, such as projection effects and variations in the orbital parameters (e.g.yelocity dispersion anisotropy profiles; see Capasso et l. 2019). These include a difference between the projected 2D clustercentric distance and the actual 3D distance and a mix of infalling and outfalling (e.g., backsplash and mere interlopers) populations in the projected phase space.

Cluster simulations (Gill et al. 2005; Rhee et al. 2017) have demonstrated thatthe line-of-sight velocity distribution of backsplash galaxies, which have passed the first pericenter and are currently outbound, overlap with the infalling galaxies at a low-velocity regime (□400 km¹) in the cluster outskirts (1–2 R₂₀₀; see,i.e., Figure 8 of Gill et al. 2005). These backsplash populations are thus likely mixed with the infalling galaxies in the projected phase space.

As a result, such sourcesof uncertainty in the projected phase space possibly cause a moderate spread ($\square 1.5 \text{ Gyr}$) in the mean infall time of each infall zonebased on the comparison with the cluster simulation at z = 0 (see, i.e., Table 1 and Figure A1 of Pasqualiet al. 2019; Smith et al. 2019; Rhee et al. 2017, 2020). Nevertheless such a comparison clearly shows that the mean infall time of each infall zone continuously increases from recer(+2.7 Gyr) to early (~5 Gyr) infallers. This suggests that (1) the projected phase space is indeed a powerful tool to study the average properties of cluster galaxies as a function of infall time, and (2) projected radial studies can only be more affected by these projection effects than phase space studies. More importantly, we note that these sources of uncertainty only make the trends in Figures 4, 6, 8, and 9 shallower, which means that the trends would be more significant if there were no such sources of uncertainty.

5. Summary and Conclusions

We have investigated environmental quenching effects using a large sample of clusters over a wide span of redshift. A uniform set of clusters and spectroscopically confirmed membergalaxies enables us to study the quenching effects kinematically by measuring the average time speintcluster environments spanning a huge range in cosmic time of \sim 5.2 Gyr, up to z \sim 1 (0.26 < z < 1.13). For that, we have mapped the location of galaxies in the cluster phase space diagram to their mean infall time.

We found that the age-sensitive 4000 Å break (2000) of galaxies continuously increases with infaltime proxy. This meansthat galaxies that spent a longer time in the cluster environment are guenched earlier, likely due to longer exposure to environmental effects such ram pressure stripping and strangulation. The most notable findings are summarized as follows.

1. We utilize the projected phase space (i.e.lustercentric radius, r_{pro}/r_{500} , versus normalized line-of-sightvelocity, $\Delta v/\sigma_{cl}$) of cluster galaxies over a large redshift baseline (z = 0.26-1.13) o estimate the galaxies kine-105 clusters (median mass of 4.97 ×110M_e) and 1626 cluster galaxies from the SPT-SZ and ACT-SZ cluster

- surveys and the optical follow-ups (Figure 1 and Table 1).
- 2. We classify galaxies by their infall time proxy. Specifically, we use the caustic profiles of the phase space (i.e., the lines of constant $(|r_{500}| \times (|\Delta v|/\sigma_{cl}))$ as the infall time proxy to split the galaxies into early, intermediate, and recent infallers (Section 3.2). The early and intermediate infallers are found to be gravitationally bound by the potential well of clusters, while recent infallers are either gravitationally bound or approaching the boundary,based on the comparison with the escape velocity radial profile of typical clusters (Figure 3).
- 3. Notably, a continuous D_n4000 (proxy for stellar age) increase with infall proxy (from recento early infall) is found in galaxies at all redshifts, z = 0.26-1.13(Figure 4). The increase in the mean D_n4000 is statistically significant, showing an increase from 1.51 ± 0.01 to 1.62 ± 0.01 . This indicates that early infall populations are, on average, ~0.71 ± 0.4 Gyr older than their recent infall counterpartsbased on the net $D_{p}4000$ increase ($\Delta D_{p}4000$) of the mean $D_{p}4000$ strengths of recent to early infall populations and simple stellar population modeling (Section 4.1)This trend is consistentwith a higher fraction of quiescentgalaxies having smaller infall time proxy values, i.e., having spent more time in the cluster environments (Figure 5). This suggests that galaxies that spent a longer time in hosts are quenched earlier, likely due to longer exposure to environmentaleffects (e.g.,ram pressure stripping and strangulation) Compared to the typicallynamical timescales of 1–3 Gyr of cluster galaxies (e.g., Rhee et al. 2020), the quenching age in our sample galaxies is small (i.e., 0.71 ± 0.4 Gyr), which is qualitatively consistent with a slow quenching starvation process (e.gLarson et al. 1980) and/or the known "delayed-then-rapid" quenching process (e.g., Wetzel et al. 2013; Haines et al. 2015; Gallazzi et al2021).
- 4. The quenching trend with infall proxy is found regardless of specific galaxy luminosity and redshifbins. Specifically, both the faint (sub-L) and bright (super-L) subsamplesshow the continuous increase of mean D_n4000 strengths with infallproxy (Figure 6). This still holds when the subsamples are further divided into lowand high-z bins (Figure 9) and is also supported by the similar gradient (slope α) of Q4000 versus infall proxy relation across all redshift and luminosity bins (Table 3). However, the exact D_n4000 strengths at a fixed infall proxy (fixed environmental effect) depend on galaxy luminosity and redshift. That is, bright galaxies show larger D_n4000 than faint galaxies for any redshiftbins, and low-z galaxies show larger \$\mathbb{A}000\$ than the high-z counterparts for any luminosity binsThis indicates that while galaxies experience environmental guenching since infall, their absolute mean age at fixed environmental effect depends on internalmass (luminosity) quenching (Figure 8 and Section 4.2) and the redshietvolution of the star-forming main sequence (Section 4.3).

This work substantially extends previous findings and provides crucial evidence for the environmental quenching matic infall stages (Figures 2 and 3). For that, we sample effects at play outside the localUniverse. Our findings were uniquely achieved by using both a wide range of redshift and the time-averaged kinematic approach in a uniformly selected sample of clusters with nearly flatnass sensitivityAdditionally, our results demonstrate a continuous 4000 increase of galaxies with infall time proxy, in good agreement with cluster simulations that show the systematic gas stripping and quenching of galaxies since infall. Future studies of the gas properties of these high-z cluster galaxies combined with the phase space analysis will provide additional insights on environmental effects at high redshifts.

Acknowledgments

We thank the referee for constructive comments that improved the quality of the paper. This work was performed in the context of the South Pole Telescope scientific program. The SPT is supported by the National Science Foundation through grantOPP-1852617Partial supportis also provided by the Kavli Institute of Cosmological Physics at the University Fagotto, F., Bressan A., Bertelli, G., et al. 1994, A&AS, 104, 365 of Chicago. PISCO observations are supported by NSF AST-1814719. Argonne National Laboratory's work was supported by the U.S. Department of Energy, Office of High Energy Physics, under contract DE-AC02-06CH11357. G.M. acknowl edges funding from the European Union's Horizon 2020 research and innovation program underMarie Skodowska-Curie grant agreement No. MARACAS - DLV-896778. A.S. is supported by ERC-StG "ClustersXCosmo" grantagreement 716762. FARE-MIUR grant 'ClustersXEuclid' R165SBKTMA, and the INFN InDark Grant. The Melbourne group acknowledgessupport from the Australian Research Council's Discovery Projects scheme (DP200101068).

ORCID iDs

Keunho J.Kim https://orcid.org/0000-0001-6505-0293
Matthew B. Baylissh https://orcid.org/0000-0003-1074-4807
Allison G. Nobleh https://orcid.org/0000-0003-1832-4137
Gourav Khullarh https://orcid.org/0000-0002-3475-7648
Ethan Cronkh https://orcid.org/0000-0003-0700-4496
Behzad Ansarinejad https://orcid.org/0000-0002-6443-3396

Benjamin Floyd[®] https://orcid.org/0000-0003-4175-571X Guillaume Mahler[®] https://orcid.org/0000-0003-3266-2001 Michael A. McDonald[®] https://orcid.org/0000-0001-5226-8349

Christian L. Reichardt https://orcid.org/0000-0003-2226-9169

Alexandro Saro https://orcid.org/0000-0002-9288-862X Keren Sharo https://orcid.org/0000-0002-7559-0864 Taweewat Somboonpanyakulhttps://orcid.org/0000-0003-3521-3631

Veronica Strazzullo https://orcid.org/0000-0001-7975-2894

References

```
Abadi, M. G., Moore, B., & Bower, R. G. 1999, MNRAS, 308, 947
Adams, N. J., Bowler, R. A. A., Jarvis, M. J., et al. 2021, MNRAS, 506, 4933
Balogh, M. L., Morris, S. L., Yee, H. K. C., et al. 1999, ApJ, 527, 54
Balogh, M. L., Navarro, J. F., & Morris, S. L. 2000, ApJ, 540, 113
Balogh, M. L., van der Burg, R. F. J., Muzzin, A., et al. 2021, MNRAS, 500, 358
Bayliss, M. B., Ruel, J., Stubbs, C. W., et al. 2016, ApJS, 227, 3
Bayliss, M. B., Zengo, K., Ruel, J., et al. 2017, ApJ, 837, 88
Bleem, L. E., Bocquet, S., Stalder, B., et al. 2020, ApJS, 247, 25
Bleem, L. E., Stalder, B., de Haan, T., et al. 2015, ApJS, 216, 27
Bluck, A. F. L., Maiolino, R., Brownson, S., et al. 2022, A&A, 659, A160
Bode, P., Ostriker, J. P., Cen, R., et al. 2012, arXiv:1204.1762
```

Boselli, A., Cortese, L., Boquien, M., et al. 2014a, A&A, 564, A67

```
Boselli, A., Fossati, M., & Sun, M. 2022, A&ARv, 30, 3
Boselli, A., Gavazzi, G., Donas, J., et al. 2001, AJ, 121, 753
Boselli, A., Roehlly, Y., Fossati, M., et al. 2016, A&A, 596, A11
Boselli, A., Voyer, E., Boissier, S., et al. 2014b, A&A, 570, A69
Bruzual, A. G. 1983, ApJ, 273, 105
Bruzual, G., & Charlot, S. 2003, MNRAS, 344, 1000
Bulbul, E., Chiu, I.-N., Mohr, J. J., et al. 2019, ApJ, 871, 50
Byrd, G., & Valtonen, M. 1990, ApJ, 350, 89
CapassoR., Saro, A., Mohr, J. J., et al. 2019, MNRAS, 482, 1043
Choi, E., Ostriker, J. P., Naab, T., et al. 2015, MNRAS, 449, 4105
Chung, A., van Gorkom, J. H., Kenney, J. D. P., et al. 2009, AJ, 138, 1741
Coenda, V., de los Rios, M., Muriel, H., et al. 2022, MNRAS, 510, 1934
Cortese L., Bekki, K., Boselli, A., et al. 2016, MNRAS, 459, 3574
Cortese L., Catinella, B., & Smith, R. 2021, PASA, 38, e035
Crowl, H. H., & Kenney, J. D. P. 2008, AJ, 136, 1623
Dekel, A., & Birnboim, Y. 2006, MNRAS, 368, 2
Dressler A. 1980, ApJ, 236, 351
Ebeling, H., Stephenson,L. N., & Edge, A. C. 2014, ApJL, 781, L40
Ettori, S., & Balestra, I. 2009, A&A, 496, 343
Fakhouri, O., Ma, C.-P., & Boylan-Kolchin, M. 2010, MNRAS, 406, 2267
                   SJ,56, 29
Fumagalli, M., Krumholz, M. R., Prochaska, J. X., et al. 2009, ApJ, 697, 1811
Gallazzi, A. R., Pasquali, A., Zibetti, S., et al. 2021, MNRAS, 502, 4457
Gavazzi, G., Consolandi, G., Gutierrez, M. L., et al. 2018, A&A, 618, A130
Gavazzi, G., & Scodeggio, M. 1996, A&A, 312, L29
Geller, M. J., Hwang, H. S., Fabricant, D. G., et al. 2014, ApJS, 213, 35
Gilbank, D. G., Gladders, M. D., Yee, H. K. C., et al. 2011, AJ, 141, 94
Gill, S. P. D., Knebe, A., & Gibson, B. K. 2005, MNRAS, 356, 1327
Gunn, J. E., & Gott, J. R. 1972, ApJ, 176, 1
Haines, C. P., Iovino, A., Krywult, J., et al. 2017, A&A, 605, A4
Haines, C. P., Pereira, M. J., Sanderson, A. J. R., et al. 2012, ApJ, 754, 97
Haines, C. P., Pereira, M. J., Smith, G. P., et al. 2015, ApJ, 806, 101
Hamilton, D. 1985, ApJ, 297, 371
Han, S., Smith, R., Choi, H., et al. 2018, ApJ, 866, 78
Hasselfield, M., Hilton, M., Marriage, T. A., et al. 2013, JCAP, 2013, 008
Hennig, C., Mohr, J. J., Zenteno, A., et al. 2017, MNRAS, 467, 4015
Hernán-Caballero, A., Alonso-Herrero, A., Pérez-González, P. G., et al. 2013,
         AS, 434, 2136
Hernández-Fernández, J. D., Haines, C. P., Diaferio, A., et al. 2014, MNRAS,
   438, 2186
High, F. W., Stalder, B., Song, J., et al. 2010, ApJ, 723, 1736
Hilton, M., Hasselfield, M., Sifón, C., et al. 2018, ApJS, 235, 20
Jaffé, Y. L., Poggianti, B. M., Moretti, A., et al. 2018, MNRAS, 476, 4753
Jaffé, Y. L., Smith, R., Candlish, G. N., et al. 2015, MNRAS, 448, 1715
Janz, J., Salo, H., Su, A. H., et al. 2021, A&A, 647, A80
Jung, S. L., Choi, H., Wong, O. I., et al. 2018, ApJ, 865, 156
Kauffmann, G., Heckman, T. M., White, S. D. M., et al. 2003, MNRAS,
   341,33
Kauffmann, G., White, S. D. M., Heckman, T. M., et al. 2004, MNRAS,
   353,713
Kawinwanichakij, L., Papovich, C., Quadri, R. F., et al. 2017, ApJ, 847, 134
Kelkar, K., Gray, M. E., Aragón-Salamanca, A., et al. 2019, MNRAS, 486, 868
Kenney, J. D. P., van Gorkom, J. H., & Vollmer, B. 2004, AJ, 127, 3361
Khullar, G., Bayliss, M. B., Gladders, M. D., et al. 2021, ApJ, 934, 177
Kim, K., Malhotra, S., Rhoads, J. E., et al. 2018, ApJ, 867, 118
Kim, K., Oh, S., Jeong, H., et al. 2016, ApJS, 225, 6
Larson, R. B., Tinsley, B. M., & Caldwell, C. N. 1980, ApJ, 237, 692
Lee, B., & Chung, A. 2018, ApJL, 866, L10
Lee, B., Wang, J., Chung, A., et al. 2022, ApJS, 262, 31
Liu, Q., Yee, H. K. C., Drissen, L., et al. 2021, ApJ, 908, 228
Longobardi, A., Boselli, A., Fossati, M., et al. 2020, A&A, 644, A161
Loni, A., Serra, P., Kleiner, D., et al. 2021, A&A, 648, A31
Mahajan, S., Mamon, G. A., & Raychaudhury, S. 2011, MNRAS, 416, 2882
Mamon, G. A., Sanchis, T., Salvador-Solé, et al. 2004, A&A, 414, 445
Marriage, T. A., Acquaviva, V., Ade, P. A. R., et al. 2011, ApJ, 737, 61
Matharu, J., Muzzin, A., Brammer, G. B., et al. 2021, ApJ, 923, 222
McDonald, M., Benson, B. A., Vikhlinin, A., et al. 2014, ApJ, 794, 67
McGaugh, S. S., & Schombert, J. M. 2014, AJ, 148, 77
Moore, B., Katz, N., Lake, G., et al. 1996, Natur, 379, 613
Morokuma-Matsui, K., Kodama, T., Morokuma, T., et al. 2021, ApJ, 914, 145
Muzzin, A., van der Burg, R. F. J., McGee, S. L., et al. 2014, ApJ, 796, 65
Muzzin, A., Wilson, G., Yee, H. K. C., et al. 2012, ApJ, 746, 188
Navarro, J. F., Frenk, C. S., & White, S. D. M. 1996, ApJ, 462, 563
Noble, A. G., Webb, T. M. A., Muzzin, A., et al. 2013, ApJ, 768, 118
Noble, A. G., Webb, T. M. A., Yee, H. K. C., et al. 2016, ApJ, 816, 48
```

```
Noordeh, E., Canning, R. E. A., Willis, J. P., et al. 2021, MNRAS, 507, 5272
Oh, S., Kim, K., Lee, J. H., et al. 2018, ApJS, 237, 14
Oman, K. A., Bahé, Y. M., Healy, J., et al. 2021, MNRAS, 501, 5073
Oman, K. A., & Hudson, M. J. 2016, MNRAS, 463, 3083
Oman, K. A., Hudson, M. J., & Behroozi, P. S. 2013, MNRAS, 431, 2307
Pandya, V., Brennan, R., Somerville, R. S., et al. 2017, MNRAS, 472, 2054
Park, C., & Hwang, H. S. 2009, ApJ, 699, 1595
Pasquali A., Smith, R., Gallazzi, A., et al. 2019, MNRAS, 484, 1702
Paulino-Afonso A., Sobral, D., Darvish, B., et al. 2020, A&A, 633, A70
Peng,Y.-J., Lilly, S. J., Kovač, K., et al. 2010, ApJ, 721, 193
Pintos-Castrol., Yee, H. K. C., Muzzin, A., et al. 2019, ApJ, 876, 40
Reeves, A. M. M., Balogh, M. L., van der Burg, R. F. J., et al. 2021, MNRAS,
   506, 3364
Reeves, A. M. M., Hudson, M. J., & Oman, K. A. 2023, MNRAS, 522, 1779
Reichardt, C. L., Stalder, B., Bleem, L. E., et al. 2013, ApJ, 763, 127
Rhee, J., Smith, R., Choi, H., et al. 2017, ApJ, 843, 128
Rhee, J., Smith, R., Choi, H., et al. 2020, ApJS, 247, 45
Ruel, J., Bazin, G., Bayliss, M., et al. 2014, ApJ, 792, 45
Rykoff, E. S., Koester, B. P., Rozo, E., et al. 2012, ApJ, 746, 178
Salpeter E. 1955, ApJ, 121, 161
Sampaio, V. M., de Carvalho, R. R., Ferreras, I., et al. 2021, MNRAS,
```

Shen, L., Lemaux, B. C., Lubin, L. M., et al. 2020, MNRAS, 494, 5374 Sifón, C., MenanteauF., HasselfieldM., et al. 2013, ApJ, 772, 25 Smith, R., Pacifici, C., Pasquali A., et al. 2019, ApJ, 876, 145 Smith, R. J., Lucey, J. R., Price, J., et al. 2012, MNRAS, 419, 3167 Sobral, D., Best, P. N., Smail, I., et al. 2014, MNRAS, 437, 3516 Sobral, D., van der Wel, A., Bezanson R., et al. 2022, ApJ, 926, 117 Stalder, B., Stark, A. A., Amato, S. M., et al. 2014, Proc. SPIE, 9147, 91473Y Strazzullo, V., Gobat, R., Daddi, E., et al. 2013, ApJ, 772, 118 Strazzullo, V., Pannella, M., Mohr, J. J., et al. 2019, A&A, 622, A117 Sunyaev,R. A., & Zeldovich, Y. B. 1972, CoASP,4, 173 Tiley, A. L., Vaughan, S. P., Stott, J. P., et al. 2020, MNRAS, 496, 649 Upadhyay, A. K., Oman, K. A., & Trager, S. C. 2021, A&A, 652, A16 Vanderlinde, K., Crawford, T. M., de Haan, T., et al. 2010, ApJ, 722, 1180 Vaughan, S. P., Tiley, A. L., Davies, R. L., et al. 2020, MNRAS, 496, 3841 Vollmer, B., Cayatte, V., Balkowski, C., et al. 2001, ApJ, 561, 708 Webb, K., Balogh, M. L., Leja, J., et al. 2020, MNRAS, 498, 5317 Werner, S. V., Hatch, N. A., Muzzin, A., et al. 2022, MNRAS, 510, 674 Wetzel, A. R., Tinker, J. L., Conroy, C., et al. 2013, MNRAS, 432, 336 Whitaker, K. E., van Dokkum, P. G., Brammer, G., et al. 2012, ApJL, 754, L29 Yoon, H., Chung, A., Smith, R., et al. 2017, ApJ, 838, 81